

Transiting Exoplanet Monitoring Project (TEMP). VI. The Homogeneous Refinement of System Parameters for 39 Transiting Hot Jupiters with 127 New Light Curves

XIAN-YU WANG ,^{2,3} YONG-HAO WANG ,¹ SONGHU WANG ,⁴ ZHEN-YU WU ,^{2,3} MALENA RICE ,⁵ XU ZHOU,² TOBIAS C. HINSE ,^{6,7} HUI-GEN LIU ,⁸ BO MA ,¹ XIYAN PENG,² HUI ZHANG ,^{8,9} CONG YU ,¹ JI-LIN ZHOU ,⁸
 AND GREGORY LAUGHLIN 

¹*School of Physics and Astronomy, Sun Yat-Sen University, Zhuhai, 519082, China*

²*National Astronomical Observatories, Chinese Academy of Sciences, Beijing 100012, China*

³*University of Chinese Academy of Sciences, Beijing, 100049, China*

⁴*Department of Astronomy, Indiana University, Bloomington, IN 47405, USA*

⁵*Department of Astronomy, Yale University, New Haven, CT 06511, USA*

⁶*Institute of Astronomy, Faculty of Physics, Astronomy and Informatics, Nicolaus Copernicus University, Grudziadzka 5, 87-100 Torun, Poland*

⁷*Chungnam National University, Department of Astronomy, Space Science & Geology, 34134 Daejeon, Republic of Korea*

⁸*School of Astronomy and Space Science and Key Laboratory of Modern Astronomy and Astrophysics in Ministry of Education, Nanjing University, Nanjing 210093, China*

⁹*Shanghai Astronomical Observatory, Chinese Academy of Sciences, Shanghai 200030, China*

Submitted to ApJS

ABSTRACT

We present 127 new transit light curves for 39 hot Jupiter systems, obtained over the span of five years by two ground-based telescopes. A homogeneous analysis of these newly collected light curves together with archived spectroscopic, photometric, and Doppler velocimetric data using EXOFASTv2 leads to a significant improvement in the physical and orbital parameters of each system. All of our stellar radii are constrained to accuracies of better than 3%. The planetary radii for 37 of our 39 targets are determined to accuracies of better than 5%. Compared to our results, the literature eccentricities are preferentially overestimated due to the Lucy-Sweeney bias. Our new photometric observations therefore allow for significant improvement in the orbital ephemerides of each system. Our correction of the future transit window amounts to a change exceeding 10 min for ten targets at the time of JWST’s launch, including a 72 min change for WASP-56. The measured transit mid-times for both literature light curves and our new photometry show no significant deviations from the updated linear ephemerides, ruling out in each system the presence of companion planets with masses greater than $0.39 - 5.0 M_{\oplus}$, $1.23 - 14.36 M_{\oplus}$, $1.65 - 21.18 M_{\oplus}$, and $0.69 - 6.75 M_{\oplus}$ near the 1:2, 2:3, 3:2, and 2:1 resonances with the hot Jupiters, respectively, at a confidence level of $\pm 1\sigma$. The absence of resonant companion planets in the hot Jupiter systems is inconsistent with the conventional expectation from disk migration.

Keywords: planets and satellites: fundamental parameters — stars: fundamental parameters — techniques: photometric

1. INTRODUCTION

Xian-Yu Wang
 xianyu_wang@nao.cas.cn

Yong-Hao Wang
 wangyaho5@mail.sysu.edu.cn

Thousands of exoplanets have been detected to date; among them, transiting hot Jupiters are the most observationally accessible class of exoplanets and hence provide the highest signal-to-noise data (see, e.g., new discoveries from the Transiting Exoplanet Survey Satellite (TESS): Wang et al. 2019; Cañas et al. 2019; Jones et al. 2019; Addison et al. 2020; Brahm et al. 2020; Davis

et al. 2020; Jordán et al. 2020). These transiting “hot Jupiters” provide us with unique laboratories to test theories of exoplanet formation and evolution with relatively high precision over short time scales.

The frequency of a planet’s transits encodes the orbital period, and the depth of these transits encodes the planetary radius, assuming we know the stellar radius. A combination of photometric radius measurements and Doppler mass determinations enables us to measure the bulk density of exoplanets, helping us to understand what they are made of and how they formed. Some hot Jupiters have unusually low densities by comparison with the expected values from structural models (Laughlin et al. 2011). The dominant mechanism that slows down their convective cooling is still poorly known (Thorngren & Fortney 2018).

Moreover, transiting hot Jupiters around bright stars enable the study of their stellar obliquities via the Rossiter-McLaughlin effect (Holt 1893; Schlesinger 1910; Rossiter 1924; McLaughlin 1924; Queloz et al. 2000; Hébrard et al. 2008; Albrecht et al. 2012; Zhou et al. 2016; Wang et al. 2018a; Addison et al. 2018; Winn & Fabrycky 2015 and references within), planetary atmospheres using transmission spectroscopy (Charbonneau et al. 2002; Kreidberg et al. 2014; Deming & Seager 2017 and references within), and thermal emission through secondary eclipses (Charbonneau et al. 2005; Deming et al. 2005) and phase variations (Borucki et al. 2009; Knutson et al. 2012). Transiting hot Jupiters around bright stars also present the opportunity to measure planetary oblateness (Carter & Winn 2010), rotation rates (Seager & Hui 2002), orbital variations (e.g. transit timing variations (TTVs), Holman et al. 2006; Millholland et al. 2016; Wu et al. 2018; orbital decay, Schlaufman & Winn 2013; Penev et al. 2018, orbital precession, Bouma et al. 2019), and planetary system architectures (Becker et al. 2015; Cañas et al. 2019; Huang et al. 2020). These observational properties afford a unique opportunity for us to understand the underlying physics of tidal and perturbation theory, as well as planet formation mechanisms.

Although the number and variety of exoplanets have been dramatically expanded by space missions (*CoRoT*, Auvergne et al. 2009; *Kepler*, Borucki et al. 2010; *K2*, Howell et al. 2014; *TESS*, Ricker et al. 2015), most of the currently known hot Jupiters were discovered by ground-based transit surveys, such as SuperWASP (Pollacco et al. 2006), HATNet (Bakos et al. 2004), HAT-South (Bakos et al. 2013), OGLE (Udalski et al. 2002), TRES (Alonso et al. 2004), QES (Alsubai et al. 2013), CSTAR (Wang et al. 2014a), KELT (Pepper et al. 2007), XO (McCullough et al. 2005), MASCARA (Talens et al.

2017), MEarth (Irwin et al. 2009), and NGTS (Wheatley et al. 2018).

Some hot Jupiters that are discovered by ground-based transit surveys receive only a handful of photometric follow-up observations. We therefore initiated a geographically dispersed Transiting Exoplanet Monitoring Project (TEMP, Wang et al. 2018b) by leveraging abundant 1m-class telescopes, to which we have access, to gather long-term, high-quality photometry for currently known hot Jupiters. Considering the target visibility, telescope size, and photometric precision that we usually achieve, we set the following three criteria for target selection: 1). Targets are above a declination of -20° ; 2). The magnitudes of targets are between $V = 7.5$ and $V = 14.5$; and 3). The planetary transit has depth > 0.005 mag. TEMP offers a powerful tool for us to achieve several goals. First, we can refine the orbital and physical parameters of the known transiting hot Jupiters discovered with ground-based photometric surveys. Second, we can identify statistically significant TTVs, which can be caused not only by planet-planet interactions (Wang et al. 2017), but also by tidal dissipation, as well as apsidal precession caused by the stellar quadrupole moment, general relativity, and long-period planetary/stellar companions (Pál & Kocsis 2008).

In this paper, we present 127 new photometric light curves for 39 transiting hot Jupiters. By jointly analyzing our light curves together with archived photometric and Doppler velocimetric data, as well as stellar information, we report refined system parameters for these targets.

This paper is organized as follows. In Section 2, we describe the new photometric observations and their reduction. Section 3 details the technique we used to estimate the system parameters. Section 4 discusses our results and their implications.

2. OBSERVATIONS AND DATA REDUCTION

We collected 127 transits for 39 hot Jupiters with the 60/90 cm Schmidt telescope and the 60 cm telescope at the Xinglong Station of the National Astronomical Observatory of China (NAOC), which lies about 75 miles (120 km) to the northeast of Beijing. A total of 23,519 exposures (~ 454 hours, spread across 102 nights) were collected between Nov 11, 2013 and May 8, 2018. Figure 1 shows the distribution of TEMP targets across the sky. The allocation of transit observations reported in this work is displayed for each target in Figure 2, described in detail in the following sections.

2.1. Xinglong 60/90 cm Schmidt Telescope

We observed 49 transits of 24 planets in *R*-band using the Xinglong 60/90 cm Schmidt telescope. The telescope

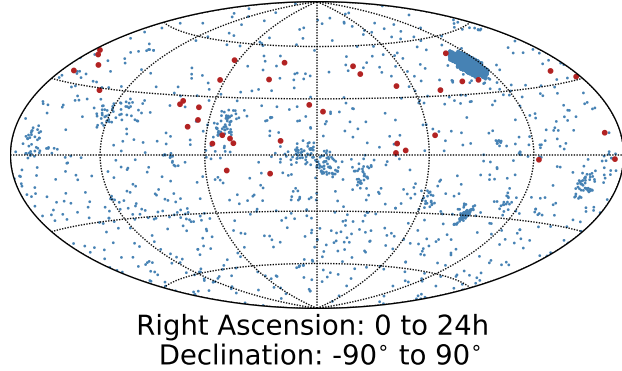


Figure 1. The distribution of observed TEMP targets (red dots). We collected 127 transit light curves for 39 hot Jupiter systems between Nov 11, 2013 and May 08, 2018. The brightest target in our sample is WASP-38 ($V = 9.48$) and the faintest one is HAT-P-53 ($V = 13.73$). All other currently known exoplanets are displayed in blue.

is equipped with a $4\text{K} \times 4\text{K}$ CCD, which gives a pixel scale of $1.38''/\text{pixel}^{-1}$ and a field of view of $94' \times 94'$. A 512×512 pixel ($\sim 12' \times 12'$) subframe was used to significantly reduce the readout time from 1.5 minutes to 4 seconds.

More details about this telescope and instrument are given by Zhou et al. (1999, 2001).

2.2. Xinglong 60 cm Telescope

We acquired 78 light curves for 33 planets in R band with the Xinglong 60 cm Telescope. Because of frequent equipment updates and tests, the Xinglong 60 cm telescope has a complicated history of CCD use. Observations taken between Jan 17, 2014 and Oct 21 2014 were conducted with a 512×512 CCD, which covers a field of view of $17' \times 17'$ with a plate scale of $1.95''/\text{pixel}^{-1}$. Observations collected during May 05 to Oct 22, 2015 or during Jun 18, 2016 to Feb 14, 2018 were performed with a $1\text{K} \times 1\text{K}$ CCD, which covers a field of view of $17' \times 17'$ with a plate scale of $0.99''/\text{pixel}^{-1}$. Observations made between Oct 23, 2015 and May 16, 2016 were obtained with a $2\text{K} \times 2\text{K}$ CCD, which covers a field of view of $36' \times 36'$ with a plate scale of $1.06''/\text{pixel}^{-1}$.

The time of each observation taken by both telescopes was automatically set to the precise current time using the GPS function. The beginning time of each exposure was recorded in the frame header using the UTC time standard, which was then converted to BJD_{TDB} as described in Eastman et al. (2010). To avoid non-linear effects of the CCD, the defocusing technique, which increases the duty cycle of observations to reduce the Poisson and the scintillation noise (Southworth et al. 2009), was used for bright stars. The data were reduced fol-

lowing a standard photometric procedure described in Wang X. et al. (2018), Wang et al. (2018a,b), Wang Y et al. (2017), and Wang Y. et al. (2019). We first applied standard bias and flat-field corrections to all frames, then performed aperture photometry using SExtractor (Bertin & Arnouts 1996). We identified the best aperture for both the target and reference stars as the one that minimized the root mean square (RMS) of the final differential light curves, which were obtained by comparing our target with several reference stars in the field. Highly discrepant points and/or linear trends presented in these light curves were removed. Furthermore, we quantified the quality of each light curve by its photometric noise rate (pnr ; Fulton et al. 2011), which is defined as

$$pnr = \frac{\text{rms}}{\sqrt{\Gamma}} \quad (1)$$

where the rms is the root mean square of the fitting residuals and Γ is the median number of exposures per minute. Then, using the K-means clustering method (MacQueen 1967), the light curves were divided into three groups: golden, mediocre, and bad. The results of the classification show that there are four bad light curves, including HAT-P-37 on May 31 2017; WASP-36 on Mar 02 2016; and WASP-37 on Mar 26 2017 and on Apr 20 2018. We present these bad light curves in Table 1 but did not include them in the light curve fit. A summary of the observations is provided in Table 1. The final light curves are presented in Table 2 and shown in Figure 3.

3. LIGHT CURVE ANALYSIS

3.1. Planetary System Parameters from Global Analysis

To refine the system parameters for our observed hot Jupiters, we used EXOFASTv2 (Eastman et al. 2013; Eastman 2017; Eastman et al. 2019) to simultaneously fit all published Doppler velocimetric and photometric data together with our newly collected light curves for each system. EXOFASTv2 enables simultaneous modeling of multi-band transits and multi-set radial velocities by combining the AMOEBA symplectic solver with a differential evolution Markov chain Monte Carlo (DE-MCMC; Ter braak 2006) algorithm.

For each system, we adopted Gaussian priors from the Exoplanet Orbit Database¹ for T_{eff} , [Fe/H], transit mid-times (T_0), and orbital period (P). We imposed priors on the quadratic limb-darkening coefficients from Claret (2018) based on T_{eff} , [Fe/H], and filter wave-

¹ <http://exoplanets.org/>

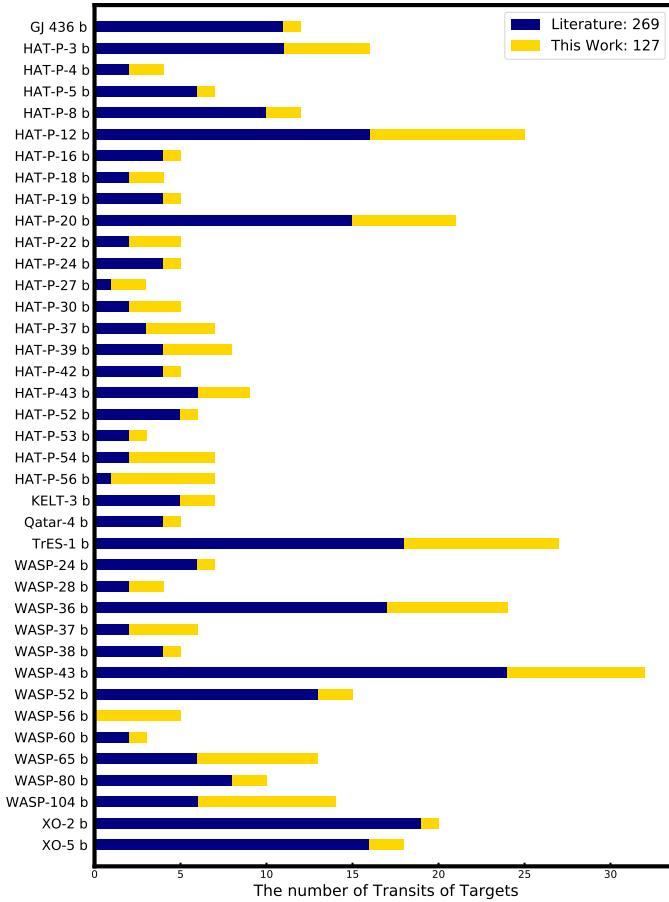


Figure 2. The number of transit light curves we used in this study (396 in total). The blue bar represents the number of archived photometric transits for each target (269 in total). The yellow bar represents the number of transits that we collected (127 in total).

length. We applied the Gaussian prior on stellar parallax to the corrected Gaia DR2 parallax (Gaia Collaboration et al. 2018; Stassun & Torres 2018). We constrained the V -band extinction (A_V) for each system by using the galactic dust maps presented in Schlafly & Finkbeiner (2011). We also used stellar isochrones from the MESA Isochrones & Stellar Tracks (MIST) catalog and constructed spectral energy distributions (SEDs) from a series of photometric catalogs² to estimate the host stellar parameters.

² Galex (Bianchi et al. 2011), Tycho-2 (Høg et al. 2000), UCAC4 (Zacharias et al. 2012), APASS (Henden et al. 2016), 2MASS (Cutri et al. 2003), WISE (Cutri & Et 2013), Gaia (Gaia Collaboration et al. 2016), the Kepler INT Survey (Greiss et al. 2012), the UBV Photoelectric Catalog (Mermilliod 1994), and the Stroemgren-Crawford uvby photometry catalog (Paunzen 2015).

All the fittings were converged by the Gelman-Rubin diagnostic (< 1.01 , Gelman & Rubin 1992). All of our new light curves and phased-folded Doppler velocities are compared in Figure 3 and Figure 4 to the respective best-fitting models.

3.2. Transit Mid-Times from Individual Fitting

Following the routine described in Wang X. et al. (2018), we used the JKTEBOP tool (Southworth et al. 2004a,b) to fit each observed transit and to subsequently derive the associated transit mid-times. For each target, we fixed all global parameters to the results derived from the global fitting in Section 3.1. The transit mid-time (T_0) and baseline flux (F_0) are the only two free parameters that we fit.

The best-fitting transit mid-times for each target were obtained by using the Levenberg-Marquardt non-linear least-squares fitting algorithm (Press et al. 1992). To obtain reliable uncertainties for the transit mid-times, the bootstrapping method, Monte Carlo simulations, and the residual-shift method were each employed independently. We chose the largest uncertainty derived from the above three methods for a conservative estimate.

The resulting transit mid-times for each target are reported in Table 3. Based on the transit mid-times, we derived the updated linear orbital ephemerides for each target using the weighted least-squares fitting algorithm. We chose the epoch in our observations that corresponds to the minimum covariance with the orbital period as the reference epoch (Mallonn et al. 2019). The deviations of transit mid-times for each target from the updated linear orbital ephemerides determined in this work are plotted in Figure 5.

4. RESULTS AND DISCUSSION

The headline result of this work is the refinement of system parameters for 39 transiting hot Jupiters. These are collected and compared to the literature results in Table 4. The stellar parameters and the most relevant planetary and orbital parameters are aggregated in Table 5 and in Table 6, respectively.

We show a comparison between system parameters from this work and from previous studies in Figure 6. Our results are based on a larger number of transits than previous measurements, so we are confident that our results with increased precision (as shown in Figure 7) are preferred over past literature values.

Stellar Physical Parameters:

Our stellar parameters are in reasonable agreement (2σ) with published results (See Panels a, b, c, d, and e in Figure 6), with the exception of a 2.6σ larger $\log g$ value derived for HAT-P-22. The derived system param-

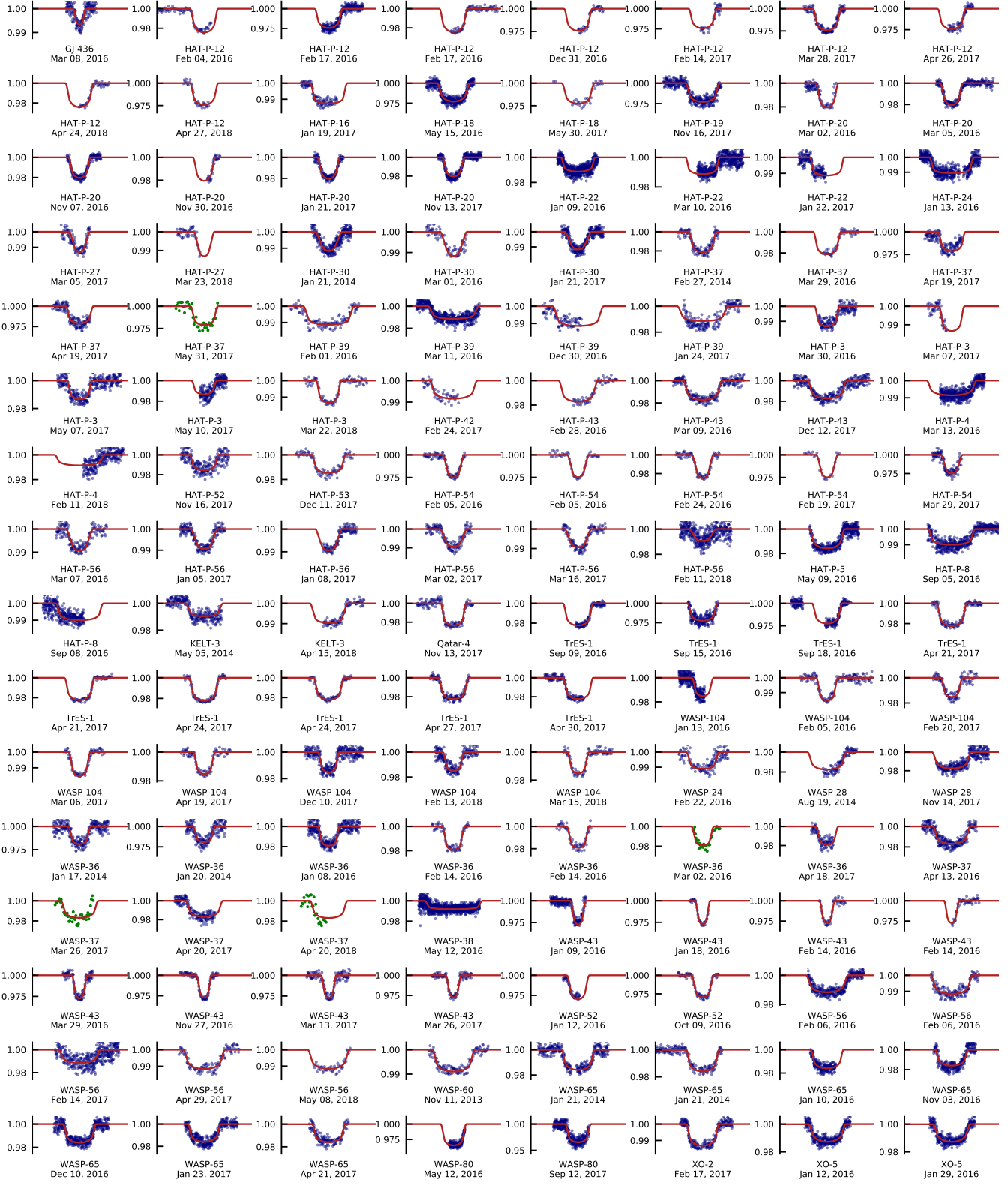


Figure 3. 127 follow-up light curves that we collected for this study. These light curves were fitted simultaneously with the archived photometric, Doppler velocimetric, and spectroscopic data to estimate the system parameters. **Four bad light curves are plotted in green.** The solid red lines show the best-fitting models.

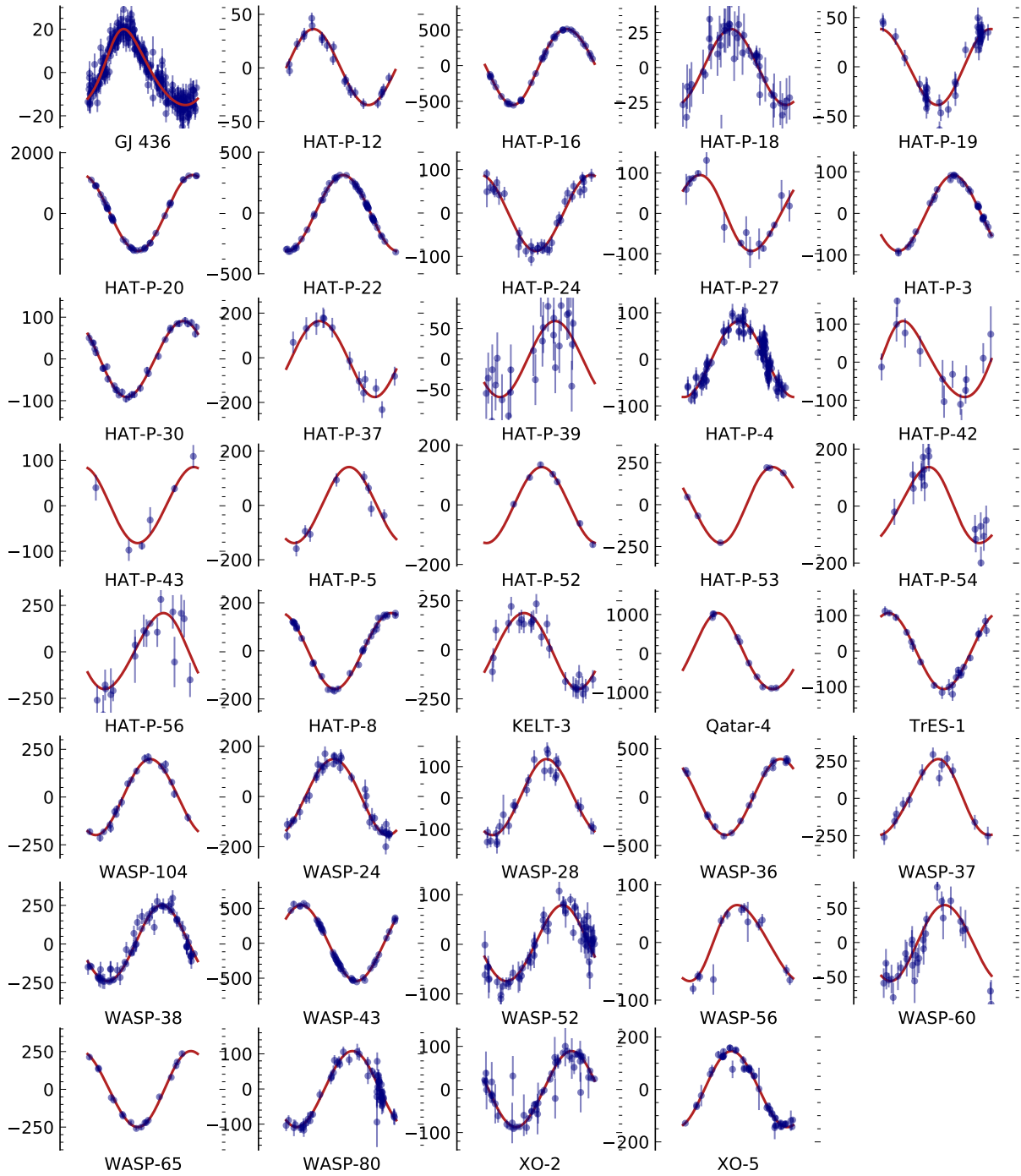


Figure 4. Archived Doppler velocimetric measurements (m/s) of our TEMP targets phase-folded with the updated orbital periods determined in this study. The best-fitting Keplerian orbital solutions from the joint radial-velocity, light-curve, and spectroscopic modeling are overplotted as solid red lines.

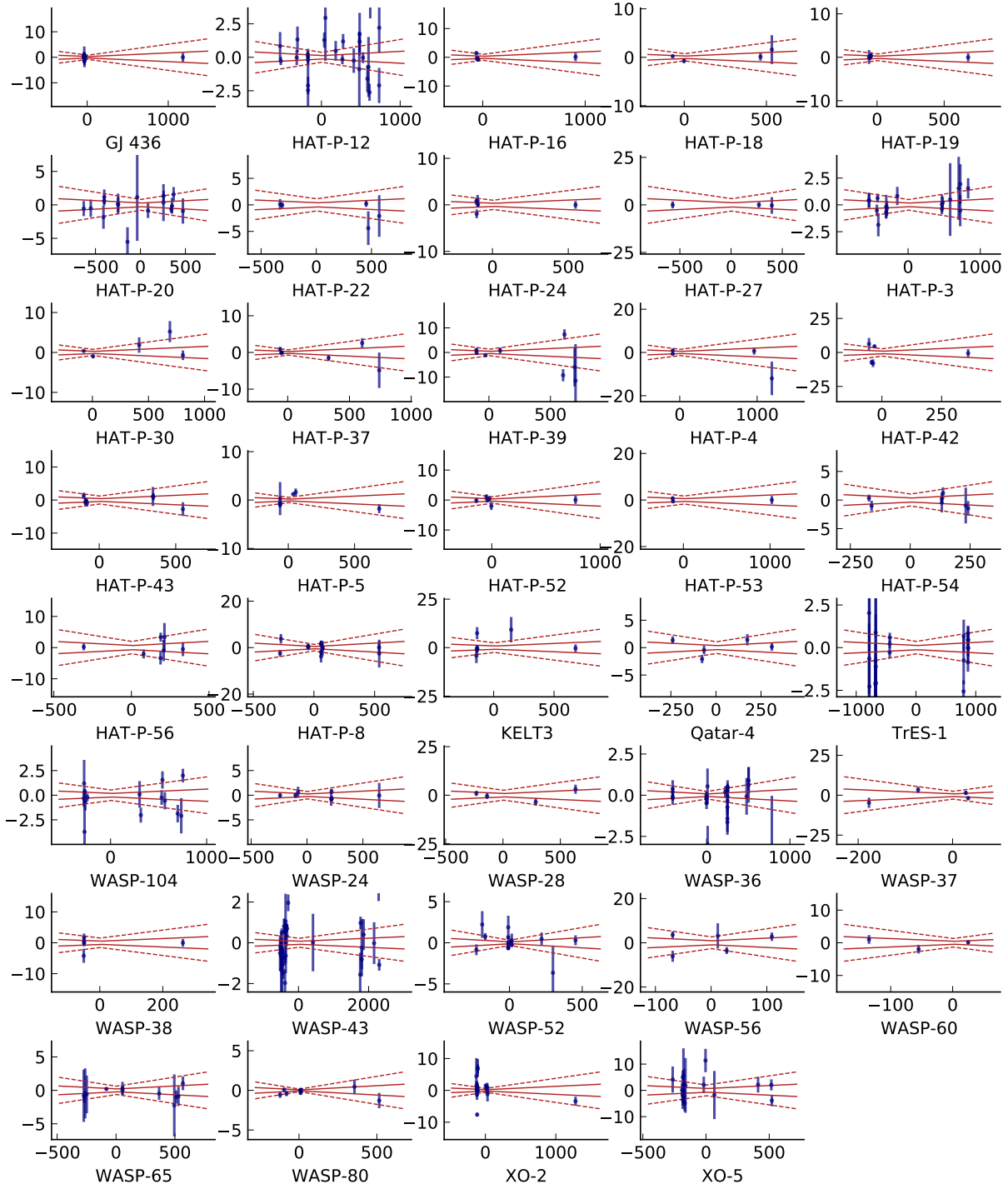


Figure 5. Transit timing variations (mins) for our targets, as compared to the best-fitting ephemerides reported in this study, shown as a function of epoch. The solid (dashed) lines indicate the propagation of $\pm 1\sigma$ ($\pm 3\sigma$) errors in the updated linear ephemerides. No statistically significant TTVs are detected in our sample at levels of $\pm 3\sigma$.

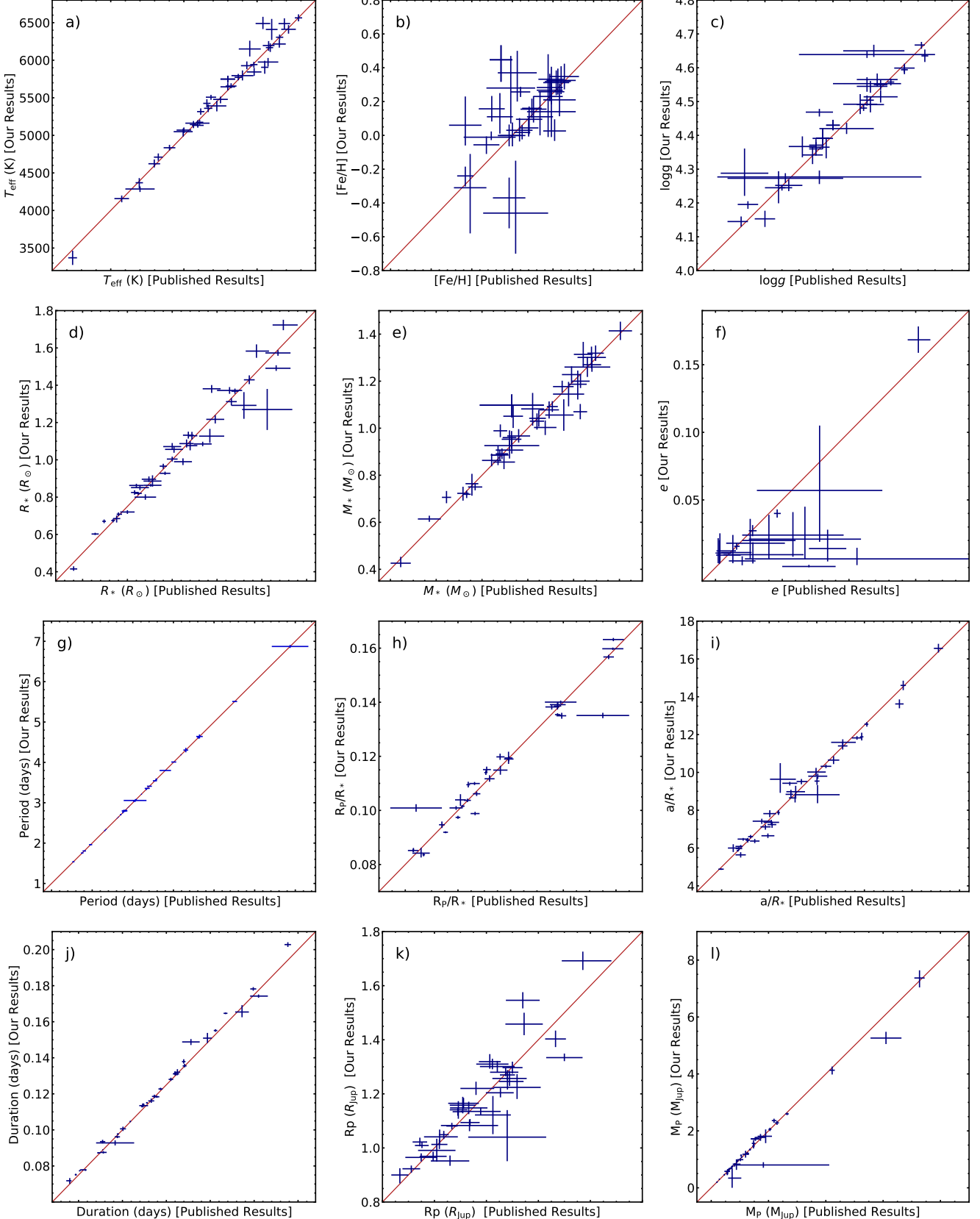


Figure 6. Comparison of the effective temperature (T_{eff} , Panel a), metallicity ($[\text{Fe}/\text{H}]$, Panel b), surface gravity ($\log g$, Panel c), stellar radius (R_* , Panel d), stellar mass (M_* , Panel e), orbital eccentricity (e , Panel f), orbital period (P , Panel g), planet-to-star radius ratio (R_p/R_* , Panel h), scaled semi-major axis (a/R_* , Panel i), transit duration (T_{14} , Panel j), planetary radius (R_p , Panel k), and planetary mass (M_p , Panel l) derived in this work and in the literature for our 39 target hot Jupiter systems. The solid lines represent exact agreement.

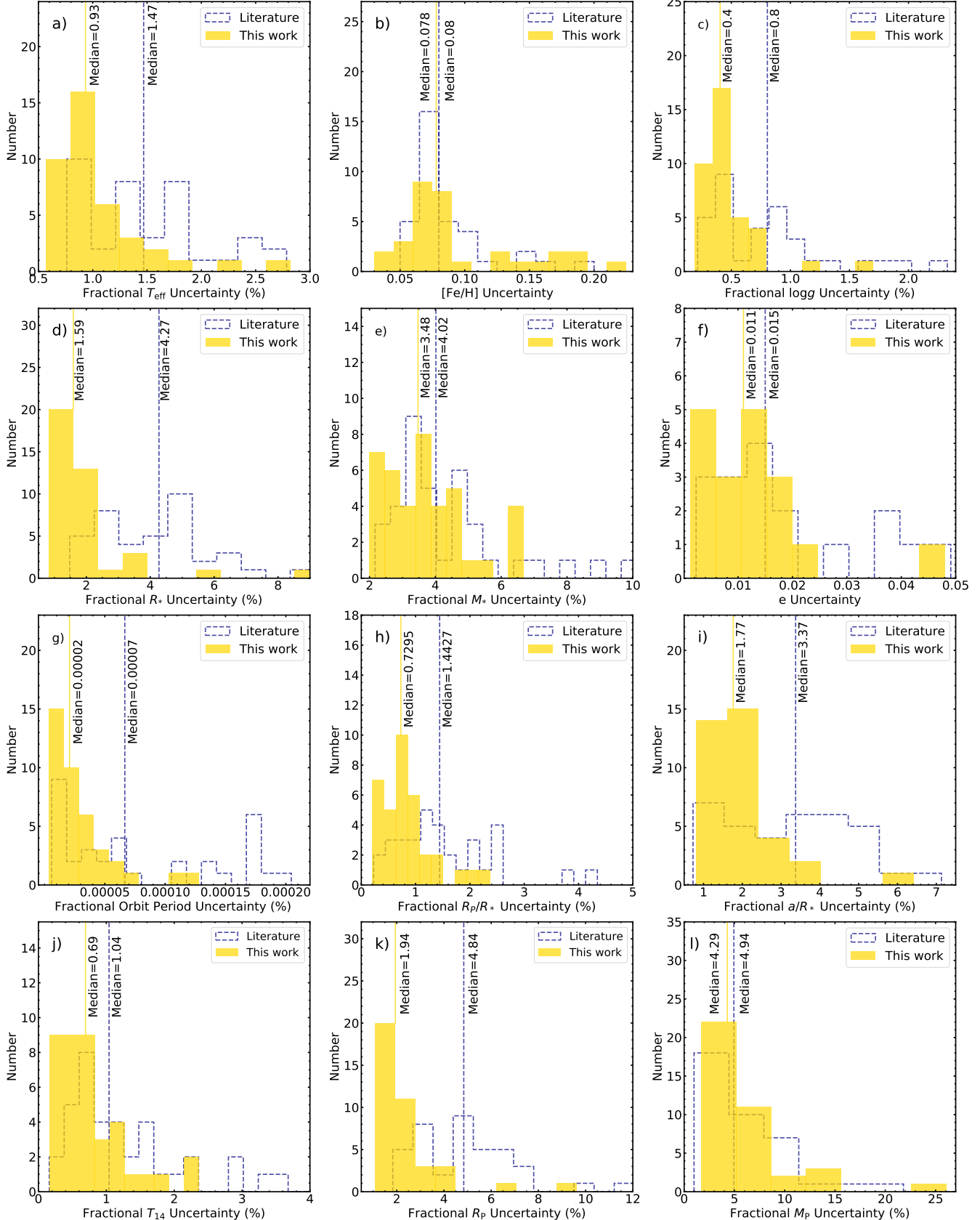


Figure 7. Distribution of uncertainties in fractional effective temperature ($\sigma_{T_{\text{eff}}}/T_{\text{eff}}$, Panel a), stellar metallicity ($\sigma_{[\text{Fe}/\text{H}]}$, Panels b), fractional surface gravity ($\sigma_{\log g}/\log g$, Panel c), fractional stellar radius (σ_{R_*}/R_* , Panel d), fractional stellar mass (σ_{M_*}/M_* , Panel e), eccentricity (σ_e , Panel f), fractional orbital period (σ_P/P , Panel g), fractional planet-to-star radius ratio ($\sigma_{R_{\text{P}}/R_*}/R_{\text{P}}/R_*$, Panel h), fractional scaled semi-major axis ($\sigma_{a/R_*}/a/R_*$, Panel i), fractional transit duration ($\sigma_{T_{14}}/T_{14}$, Panel j), fractional planetary radius ($\sigma_{R_{\text{P}}}/R_{\text{P}}$, Panel k), and fractional planetary mass ($\sigma_{M_{\text{P}}}/M_{\text{P}}$, Panel l) from this work (yellow) compared to the literature values (blue dashed line).

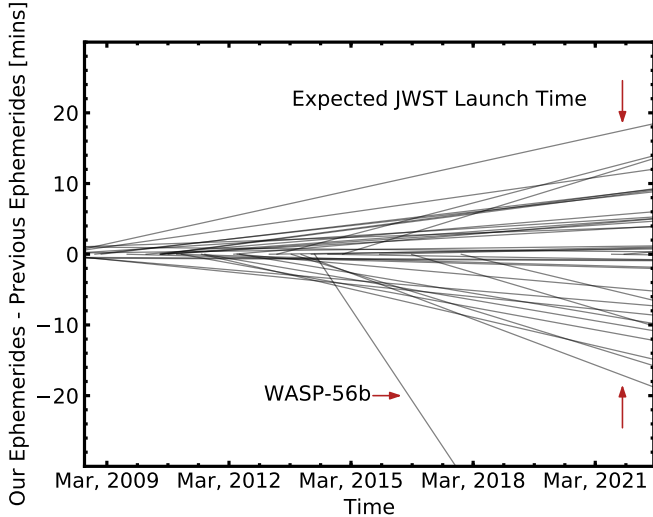


Figure 8. The difference between calculated (predicted) transit windows determined using our updated ephemerides and literature ephemerides. The difference for 29 out of 39 targets are within 10 min at the time of launch of JWST. For the other 10 targets, our predicted transit mid-times differ by more than 10 min from the literature ephemerides; for WASP-56b, the deviation amounts to about 72 min.

eters showing $> 2\sigma$ discrepancies are marked in bold in Table 4.

Although T_{eff} and $[\text{Fe}/\text{H}]$ can be independently constrained from the SED and transit limb darkening, the improvement in precision of these two parameters from our analysis is not significant (See Panels a and b in Figure 7). These parameters are typically best constrained by spectroscopic priors, while our work focuses on extending and refining the photometric baseline for the observed systems.

Compared to literature solutions, we obtained more precise $\log g$ values (See Panel c in Figure 7), since the transit alone provides an additional constraint on $\log g$ through limb darkening. We also significantly improved the precision of the host stellar radii, since a combination of the SED fits to the broad-band photometry, the upper limit on the V-band extinction from galactic dust maps, and a parallax constraint from Gaia DR2 precisely determines the bolometric luminosity and therefore stellar radius. All of our stellar radii are constrained to accuracies of better than 3% (See Panel d in Figure 7). By comparison, previous studies attained the same level of accuracy for only 28 of the 39 systems.

The transit alone provides an independent and additional constraint on the stellar density through its duration (Seager & Mallén-Ornelas 2003). The stellar mass is, therefore, more precisely constrained in our study (See Panel e in Figure 7) due to our improved stellar

radius and stellar density measurements, together with the SED fits to the broadband photometry and MIST fits to T_{eff} , $[\text{Fe}/\text{H}]$, and $\log g$.

Radial Velocity Parameters:

Since we did not obtain any new radial velocity measurements in this work, it is not surprising that the radial velocity parameters derived from our analysis typically agree with previous results in both errors and values.

Although the eccentricities that we found agree with published values within 2σ , literature studies are systematically biased towards larger eccentricities (See Panel f in Figure 6) for these nearly circular hot Jupiter systems due to the eccentricity boundary at zero (Wittenmyer et al. 2013, 2019). In this work, instead of sampling directly in e , we sample uniformly in $e \cos \omega_*$ and $e \sin \omega_*$, which helps us to reduce the Lucy-Sweeney bias (Lucy & Sweeney 1971).

Transit Parameters:

The majority of the final photometric parameters for our systems — the orbital period (P , Panel g in Figure 6 and Figure 7), the planet-to-star radius ratio (R_P/R_* , Panel h in Figure 6 and Figure 7), the scaled semi-major axis (a/R_* , Panel i in Figure 6 and Figure 7), and the transit duration (T_{14} , Panel j in Figure 6 and Figure 7) — are in agreement with but more precise than the published values.

For several systems that show $> 2\sigma$ discrepancies in the transit parameters between our analysis and previous literature values (marked in bold in Table 4), we are confident that our results are more reliable since our results are based on more extensive transit data than previous studies.

Planetary Physical Parameters:

Although we found a larger planetary radius for GJ 436 and a smaller planetary radius for HAT-P-54 compared to previous work, the planetary physical parameters (R_P and M_P) obtained in this study are generally in reasonable agreement with those from the previous literature (See Panel k and l in Figure 6), but with higher precision (see Panel k and l in Figure 7). This is especially true for planetary radius, as our results are based on more extensive photometric data. The planetary radii for almost all of our targets (37 out of 39) are determined to accuracies of better than 5%. By comparison, previous studies attained the same level of accuracy for only 21 of the 39 systems.

Transit Timing Variations:

Our new photometric observations allow for significant improvements in the orbital ephemerides (T_0 and P) of each system, which are useful to accurately predict future transit events. By 31 Oct, 2021, the currently

scheduled James Webb Space Telescope (JWST) (Gardner et al. 2006) launch date, if the literature ephemerides were left unimproved, the accumulated errors of predicted transit mid-times would exceed 1 hour for systems like WASP-56 (see Figure 8), although 29 of our 39 targets are within 10 min of previous predictions.

The refined orbital ephemerides also enable a search for TTVs. The measured transit mid-times of our targets are consistent with our updated linear ephemerides within 3σ , except for several outliers (See Figure 5). Although the origin of these outliers could be astrophysical, it is most likely that 1). The uncertainties of transit mid-times for the light curves taken under poor weather conditions are underestimated because of the presence of correlated noise or 2). The transit mid-times of very incomplete transits are imprecisely determined. Additional photometry is needed to uncover the nature of these discrepancies.

Our null results agree with previous TTV searches for hot Jupiter companion planets, conducted using both the *Kepler* dataset (Steffen et al. 2012) and ground-based photometric follow-up programs (for example: TLC, Holman et al. 2006; YETI, Neuhäuser et al. 2011; Trappsit, Gillon et al. 2012; Taste, Nascimbeni et al. 2011; TraMoS, Cortés-Zuleta et al. 2020; TEMP, Wang et al. 2018b; and Mallonn et al. 2019).

Constraints on Additional Planets:

The absence of statistically significant TTVs provides constraints on the upper mass limits for any putative companion planets in the observed hot Jupiter systems.

Using dynamical simulations with REBOUND (Rein & Liu 2012; Rein & Spiegel 2015), we searched for the masses of putative companion planets that would produce TTVs whose RMS values are the same as those measured in Section 3.2. This delineates the mass-period parameter space where additional close-in companion planets would have been detected if they existed, and, conversely, where these planets would have been remained undetected.

Our simulations assume that the putative companion planets are coplanar with the hot Jupiters, and both planets are on circular orbits. Compared with non-coplanar or eccentric orbits, the coplanar and circular configuration induces smaller TTVs and therefore provides a more conservative estimate of the putative companion planets' upper mass limits, as discussed by Agol & Deck (2016).

We stepped through the period ratio of putative companion planets and known hot Jupiters from 1:5 to 5:1 in 100 steps. The sample resolution was tripled when in proximity to resonances where the largest planetary TTVs are likely to arise (Agol et al. 2005; Hol-

man & Murray 2005). For each step, the approximated upper mass limit of the putative planet was obtained iteratively by linear interpolation with an initial mass guess of $1 M_{\oplus}$ and with a convergence tolerance of $|O_{\text{TTV RMS}} - C_{\text{TTV RMS}}| < 1 \text{ s}$.

We did not explore the TTV behavior induced by unstable putative companion planets. The regions of orbital instability were identified using the Mean Exponential Growth factor of Nearby Orbits (MEGNO $\langle Y \rangle$; Cincotta & Simó 1999, 2000; Cincotta et al. 2003; Hinse et al. 2010), which can efficiently distinguish quasi-periodic ($\langle Y \rangle \rightarrow 2$ as $t \rightarrow \infty$) or chaotic motion ($\langle Y \rangle > 2$ as $t \rightarrow \infty$). The MEGNO maps (see Figure 9) are gridded in period ratio-mass space, with 500 evenly spaced values on each axis spanning $0.1 < P_{\text{putative planet}}/P_{\text{hot Jupiter}} < 3.5$ and $10^{-2} M_{\oplus} < M_{\text{putative planet}} < 10^4 M_{\oplus}$ for the period ratio of putative companion planet and known hot Jupiter (x-axis) and mass of putative companion planet (y-axis), respectively. At each grid point, the putative companion planet was integrated together with the known hot Jupiter for 1,000 years, at which point we calculated the MEGNO factor $\langle Y \rangle$.

MEGNO also identifies the locations of mean motion resonances. As illustrated in Figure 9, the mass constraints from TTVs are more restrictive at mean-motion resonances (especially the low-order mean-motion resonances) by comparison with general orbital configurations. We rule out the presence of putative companion planets with masses greater than $0.39 - 5.00 M_{\oplus}$, $1.23 - 14.36 M_{\oplus}$, $1.65 - 21.18 M_{\oplus}$, and $0.69 - 6.75 M_{\oplus}$ near the 1:2, 2:3, 3:2, and 2:1 resonances, respectively. For a given location in a given hot Jupiter system, the upper mass limit of the putative companion planet ($m_{\text{putative planet}}$) is a function of the orbital period of the hot Jupiter (P), the TTV amplitude (Δ), and the host stellar mass (M_*), roughly scaling as $m_{\text{putative planet}} = P \cdot \Delta / M_*$. Since the systems in our sample have a similar range of stellar mass (M_* ranging from 0.426 to $1.41 M_{\odot}$) and orbital period (P ranging from 0.81 to 6.87 days), the upper limits of the putative companion planet masses are dominantly set by the TTV amplitudes (Δ ranging from 11 to 585 s) of our hot Jupiters.

The absence of nearby resonant companion planets in hot Jupiter systems is inconsistent with the conventional expectation from disk migration. Although disk migration does not provide a precise quantitative prediction of the typical occurrence rate of resonant pairs, the absence of resonant companion planets across the hot Jupiter sample, as suggested by this work and previous publications (Steffen et al. 2012; Montalto et al. 2012), strongly disfavors disk migration. This absence is compatible with violent high-eccentricity tidal migra-

tion, which ejects any original close-in companion planets. We cannot rule out *in-situ* formation, since, although *in-situ* formation tends to form hot Jupiters accompanied by nearby planets (Boley et al. 2016; Batygin et al. 2016), those planets are not necessarily in or near mean motion resonance.

A dearth of additional transit signal detections in the *Kepler* hot Jupiter sample initially appeared to place a very strong constraint on the occurrence rate of non-resonant companion planets in those systems (Steffen et al. 2012; Huang et al. 2017). However, these findings, which are generally quoted as evidence for the high-eccentricity origin of hot Jupiters, could instead result from observational bias, since the companion planets can hide in exterior and/or inclined orbits (Millholland et al. 2016), or in the observational noise. Previously hidden close-in companion planets in existing hot Jupiter systems have begun to be discovered via the transit method as better photometric precision is achieved (WASP-47, Becker et al. 2015; Kepler-730, Cañas et al. 2019; TOI-1130, Huang et al. 2020), as well as through the radial velocity method (WASP-148: Hébrard et al. 2020). These systems cannot be explained by high-eccentricity tidal migration, but they are consistent with *in-situ* formation.

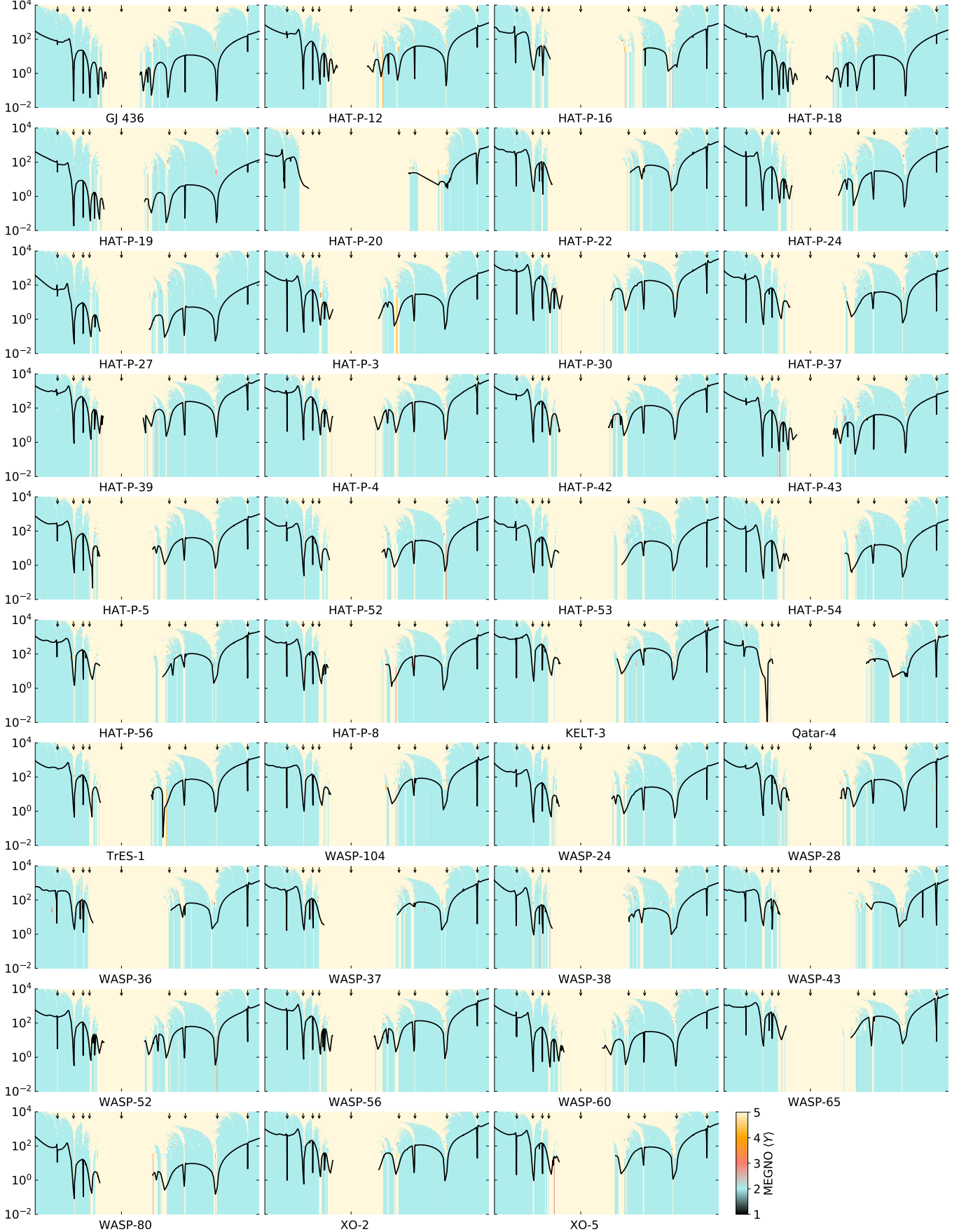


Figure 9. Upper mass limits (M_{\oplus}) as a function of the orbital period ratio of the putative companion planets and the transiting hot Jupiters. The black solid curves represent the mass-period region where putative companion planets would produce TTVs with RMS values matching those that we measured for our targets. The mass constraints are most restrictive near the low-order mean-motion resonances (marked by arrows). We use MEGNO Factor ($\langle Y \rangle$) to identify quasi-periodic regions ($\langle Y \rangle = 2$, color coded blue), as well as chaotic and possibly unstable regions ($\langle Y \rangle \neq 2$, color coded black, red, and yellow).

Table 1. Log of Observations of the TEMP Targets Presented in This Work

Planet	Date	Time	Telescope	Typical Exposure Time	N _{data}	PNR	Quality
	(UTC)	(UTC)		(s)			
GJ 436 b	Mar 08, 2016	13:17:15-15:50:10	Xinglong 60/90 cm Schmidt	40	174	0.12	Golden
HAT-P-12 b	Feb 04, 2016	17:46:07-22:19:55	Xinglong 60/90 cm Schmidt	200	76	0.32	Mediocre
	Feb 17, 2016	17:37:22-21:05:46	Xinglong 60 cm	30	323	0.15	Golden
	Feb 17, 2016	17:57:53-21:53:21	Xinglong 60/90 cm Schmidt	140	94	0.17	Golden
	Dec 31, 2016	20:25:13-22:31:45	Xinglong 60/90 cm Schmidt	150	48	0.21	Mediocre
	Feb 14, 2017	19:49:37-21:33:24	Xinglong 60/90 cm Schmidt	80	41	0.29	Mediocre
	Mar 28, 2017	12:31:25-15:59:05	Xinglong 60 cm	60	134	0.20	Mediocre
	Apr 26, 2017	12:11:48-14:18:28	Xinglong 60/90 cm Schmidt	80	73	0.27	Mediocre
	Apr 24, 2018	14:15:57-16:48:05	Xinglong 60 cm	180	44	0.21	Mediocre
	Apr 27, 2018	17:40:03-19:48:32	Xinglong 60 cm	180	36	0.25	Mediocre
HAT-P-16 b	Jan 19, 2017	10:16:44-13:17:18	Xinglong 60/90 cm Schmidt	80	106	0.13	Golden
HAT-P-18 b	May 15, 2016	12:30:12-16:33:04	Xinglong 60 cm	30	397	0.17	Golden
	May 30, 2017	14:01:18-18:10:23	Xinglong 60 cm	30	34	0.41	Mediocre
HAT-P-19 b	Nov 16, 2017	10:25:29-15:18:45	Xinglong 60 cm	25	363	0.22	Mediocre
HAT-P-20 b	Mar 02, 2016	14:41:46-17:19:44	Xinglong 60/90 cm Schmidt	60	90	0.26	Mediocre
	Mar 05, 2016	12:16:08-17:04:46	Xinglong 60/90 cm Schmidt	55	243	0.13	Golden
	Nov 07, 2016	19:09:22-22:00:40	Xinglong 60 cm	30	195	0.11	Golden
	Nov 30, 2016	20:33:31-21:37:17	Xinglong 60/90 cm Schmidt	90	35	0.16	Golden
	Jan 21, 2017	13:09:29-15:38:39	Xinglong 60 cm	30	165	0.13	Golden
	Nov 13, 2017	16:52:34-20:33:30	Xinglong 60 cm	18	321	0.13	Golden
HAT-P-22 b	Jan 09, 2016	15:27:06-18:51:35	Xinglong 60 cm	10	770	0.09	Golden
	Mar 10, 2016	17:32:40-21:23:25	Xinglong 60 cm	20	539	0.13	Golden
	Jan 22, 2017	15:49:49-18:07:29	Xinglong 60 cm	20	181	0.14	Golden
HAT-P-24 b	Jan 13, 2016	15:04:46-20:11:18	Xinglong 60 cm	20	570	0.11	Golden
HAT-P-27 b	Mar 05, 2017	17:32:14-19:57:17	Xinglong 60/90 cm Schmidt	70	94	0.21	Mediocre
	Mar 23, 2018	16:28:44-18:28:21	Xinglong 60 cm	130	47	0.23	Mediocre
HAT-P-3 b	Mar 30, 2016	12:50:45-16:02:01	Xinglong 60/90 cm Schmidt	60	180	0.19	Golden
	Mar 07, 2017	15:35:15-17:11:25	Xinglong 60/90 cm Schmidt	110	48	0.21	Mediocre
	May 07, 2017	13:13:30-18:36:43	Xinglong 60 cm	40	310	0.21	Mediocre
	May 10, 2017	12:18:24-14:34:42	Xinglong 60 cm	10	221	0.21	Mediocre
	Mar 22, 2018	12:19:33-17:37:22	Xinglong 60 cm	170	91	0.15	Golden
HAT-P-30 b	Jan 21, 2014	13:52:02-15:38:27	Xinglong 60 cm	30	299	0.13	Golden
	Mar 01, 2016	14:06:32-17:28:20	Xinglong 60/90 cm Schmidt	100	80	0.20	Golden
	Jan 21, 2017	15:43:00-19:14:28	Xinglong 60 cm	18	301	0.12	Golden
HAT-P-37 b	Feb 27, 2014	18:35:54-22:01:09	Xinglong 60 cm	90	120	0.25	Mediocre
	Mar 29, 2016	17:59:16-21:01:16	Xinglong 60/90 cm Schmidt	180	56	0.21	Mediocre
	Apr 19, 2017	17:11:22-20:22:21	Xinglong 60 cm	50	146	0.27	Mediocre
	May 31, 2017	16:09:27-19:41:51	Xinglong 60 cm	40	39	0.58	Bad

Table 1 *continued*

Table 1 (*continued*)

Planet	Date	Time	Telescope	Typical Exposure Time	N _{data}	PNR	Quality
	(UTC)	(UTC)		(s)			
HAT-P-39 b	Feb 01, 2016	11:54:55-17:38:54	Xinglong 60/90 cm Schmidt	160	109	0.28	Mediocre
	Mar 11, 2016	11:34:31-16:53:11	Xinglong 60 cm	30	529	0.16	Golden
	Dec 30, 2016	15:05:30-18:22:49	Xinglong 60/90 cm Schmidt	120	89	0.28	Mediocre
	Jan 24, 2017	11:49:28-16:40:59	Xinglong 60 cm	60	170	0.32	Mediocre
HAT-P-4 b	Mar 13, 2016	17:42:52-21:29:26	Xinglong 60 cm	20	534	0.09	Golden
	Feb 11, 2018	17:39:19-21:02:29	Xinglong 60 cm	20	254	0.24	Mediocre
HAT-P-42 b	Feb 24, 2017	15:37:30-18:40:52	Xinglong 60/90 cm Schmidt	200	55	0.19	Golden
HAT-P-43 b	Feb 28, 2016	13:40:38-17:22:45	Xinglong 60/90 cm Schmidt	200	61	0.23	Mediocre
	Mar 09, 2016	11:32:30-17:33:03	Xinglong 60 cm	80	233	0.19	Golden
	Dec 12, 2017	16:10:28-22:34:57	Xinglong 60 cm	50	307	0.24	Mediocre
HAT-P-5 b	May 09, 2016	16:08:34-20:18:52	Xinglong 60 cm	20	435	0.13	Golden
HAT-P-52 b	Nov 16, 2017	16:12:38-20:18:02	Xinglong 60 cm	40	222	0.34	Mediocre
HAT-P-53 b	Dec 11, 2017	10:22:06-15:16:34	Xinglong 60 cm	180	85	0.25	Mediocre
HAT-P-54 b	Feb 05, 2016	10:58:23-14:26:31	Xinglong 60 cm	120	93	0.19	Golden
	Feb 05, 2016	11:06:12-15:13:04	Xinglong 60/90 cm Schmidt	290	48	0.27	Mediocre
	Feb 24, 2016	11:11:08-14:51:16	Xinglong 60/90 cm Schmidt	160	78	0.23	Mediocre
	Feb 19, 2017	11:12:32-14:09:23	Xinglong 60 cm	60	25	0.39	Mediocre
	Mar 29, 2017	11:27:29-13:55:49	Xinglong 60 cm	50	110	0.30	Mediocre
HAT-P-56 b	Mar 07, 2016	11:18:29-15:34:21	Xinglong 60/90 cm Schmidt	60	165	0.12	Golden
	Jan 05, 2017	16:02:17-19:51:19	Xinglong 60/90 cm Schmidt	60	191	0.11	Golden
	Jan 08, 2017	12:37:08-15:25:31	Xinglong 60/90 cm Schmidt	70	121	0.09	Golden
	Mar 02, 2017	11:22:09-15:12:53	Xinglong 60/90 cm Schmidt	80	141	0.13	Golden
	Mar 16, 2017	11:16:49-14:54:48	Xinglong 60/90 cm Schmidt	80	121	0.14	Golden
	Feb 11, 2018	13:17:10-17:37:21	Xinglong 60 cm	10	423	0.23	Mediocre
HAT-P-8 b	Sep 05, 2016	11:43:00-17:56:37	Xinglong 60 cm	20	505	0.13	Golden
	Sep 08, 2016	12:28:56-16:00:13	Xinglong 60 cm	14	347	0.16	Golden
KELT-3 b	May 05, 2014	12:03:08-16:44:55	Xinglong 60 cm	60	265	0.23	Mediocre
	Apr 15, 2018	12:33:32-16:00:34	Xinglong 60 cm	100	92	0.09	Golden
Qatar-4 b	Nov 13, 2017	10:24:09-15:07:17	Xinglong 60 cm	100	130	0.24	Mediocre
TrES-1 b	Sep 09, 2016	12:01:48-14:30:25	Xinglong 60 cm	60	119	0.12	Golden
	Sep 15, 2016	12:26:32-14:58:10	Xinglong 60 cm	18	216	0.16	Golden
	Sep 18, 2016	11:22:10-16:27:05	Xinglong 60 cm	22	218	0.16	Golden
	Apr 21, 2017	15:58:58-20:11:03	Xinglong 60 cm	100	116	0.16	Golden
	Apr 21, 2017	16:55:05-20:22:28	Xinglong 60/90 cm Schmidt	160	73	0.13	Golden
	Apr 24, 2017	16:39:39-20:12:48	Xinglong 60 cm	100	93	0.12	Golden
	Apr 24, 2017	16:43:20-20:17:45	Xinglong 60/90 cm Schmidt	160	76	0.16	Golden
	Apr 27, 2017	17:06:20-20:26:14	Xinglong 60/90 cm Schmidt	80	132	0.16	Golden
	Apr 30, 2017	16:57:51-20:18:08	Xinglong 60/90 cm Schmidt	70	145	0.14	Golden
WASP-104 b	Jan 13, 2016	20:14:32-22:24:53	Xinglong 60 cm	15	367	0.12	Golden
	Feb 05, 2016	15:40:51-21:46:28	Xinglong 60/90 cm Schmidt	120	144	0.17	Golden

Table 1 *continued*

Table 1 (*continued*)

Planet	Date	Time	Telescope	Typical Exposure Time	N _{data}	PNR	Quality
	(UTC)	(UTC)		(s)			
	Feb 20, 2017	14:33:04-18:14:48	Xinglong 60/90 cm Schmidt	110	111	0.22	Mediocre
	Mar 06, 2017	15:48:40-19:12:57	Xinglong 60/90 cm Schmidt	120	73	0.15	Golden
	Apr 19, 2017	12:26:07-16:36:06	Xinglong 60/90 cm Schmidt	160	80	0.18	Golden
	Dec 10, 2017	17:44:45-22:39:58	Xinglong 60 cm	30	325	0.17	Golden
	Feb 13, 2018	17:01:06-20:38:11	Xinglong 60 cm	25	208	0.20	Golden
	Mar 15, 2018	13:33:15-17:38:18	Xinglong 60 cm	139	83	0.17	Golden
WASP-24 b	Feb 22, 2016	17:57:38-22:08:20	Xinglong 60/90 cm Schmidt	80	124	0.26	Mediocre
WASP-28 b	Aug 19, 2014	15:16:26-18:06:52	Xinglong 60 cm	90	102	0.24	Mediocre
	Nov 14, 2017	11:05:38-15:30:57	Xinglong 60 cm	25	313	0.23	Mediocre
WASP-36 b	Jan 17, 2014	14:39:45-19:20:42	Xinglong 60 cm	60	264	0.29	Mediocre
	Jan 20, 2014	17:07:56-20:31:16	Xinglong 60 cm	60	188	0.36	Mediocre
	Jan 08, 2016	15:45:33-20:07:08	Xinglong 60 cm	40	337	0.22	Mediocre
	Feb 14, 2016	13:10:45-16:17:46	Xinglong 60 cm	150	69	0.21	Mediocre
	Feb 14, 2016	13:11:30-16:05:21	Xinglong 60/90 cm Schmidt	160	60	0.27	Mediocre
	Mar 02, 2016	12:01:44-14:19:24	Xinglong 60/90 cm Schmidt	250	33	0.47	Bad
	Apr 18, 2017	11:51:53-13:43:47	Xinglong 60 cm	50	92	0.29	Mediocre
WASP-37 b	Apr 13, 2016	15:50:06-20:26:14	Xinglong 60 cm	55	249	0.22	Mediocre
	Mar 26, 2017	16:37:22-19:50:35	Xinglong 60 cm	40	43	0.72	Bad
	Apr 20, 2017	17:13:06-20:38:04	Xinglong 60 cm	40	180	0.21	Mediocre
	Apr 20, 2018	15:02:26-17:08:44	Xinglong 60 cm	249	26	0.71	Bad
WASP-38 b	May 12, 2016	17:31:50-17:31:32	Xinglong 60 cm	12	1056	0.11	Golden
WASP-43 b	Jan 09, 2016	19:42:49-22:43:56	Xinglong 60 cm	45	219	0.2	Golden
	Jan 18, 2016	19:42:52-21:18:44	Xinglong 60 cm	150	38	0.15	Golden
	Feb 14, 2016	16:24:49-18:37:08	Xinglong 60 cm	150	51	0.27	Mediocre
	Feb 14, 2016	17:07:08-19:24:23	Xinglong 60/90 cm Schmidt	160	49	0.30	Mediocre
	Mar 29, 2016	13:55:29-16:27:52	Xinglong 60/90 cm Schmidt	60	126	0.22	Mediocre
	Nov 27, 2016	18:46:02-22:01:22	Xinglong 60/90 cm Schmidt	100	98	0.18	Golden
	Mar 13, 2017	13:01:32-16:40:18	Xinglong 60/90 cm Schmidt	90	118	0.30	Mediocre
	Mar 26, 2017	13:23:27-16:47:56	Xinglong 60/90 cm Schmidt	100	111	0.19	Golden
WASP-52 b	Jan 12, 2016	10:17:30-11:42:14	Xinglong 60 cm	100	49	0.32	Mediocre
	Oct 09, 2016	14:39:28-18:06:37	Xinglong 60/90 cm Schmidt	150	77	0.21	Mediocre
WASP-56 b	Feb 06, 2016	16:37:17-21:21:43	Xinglong 60 cm	45	333	0.13	Golden
	Feb 06, 2016	16:29:28-20:34:20	Xinglong 60/90 cm Schmidt	90	141	0.19	Golden
	Feb 14, 2017	15:44:07-21:09:08	Xinglong 60 cm	15	375	0.29	Mediocre
	Apr 29, 2017	12:31:36-17:37:16	Xinglong 60/90 cm Schmidt	140	104	0.24	Mediocre
	May 08, 2018	13:04:20-16:09:08	Xinglong 60 cm	249	45	0.23	Mediocre
WASP-60 b	Nov 11, 2013	10:38:18-15:40:59	Xinglong 60/90 cm Schmidt	100	125	0.12	Golden
WASP-65 b	Jan 21, 2014	15:45:12-21:41:30	Xinglong 60 cm	60	302	0.17	Golden
	Jan 21, 2014	14:29:34-20:47:23	Xinglong 60/90 cm Schmidt	80	180	0.17	Golden
	Jan 10, 2016	14:09:05-16:17:48	Xinglong 60 cm	30	213	0.12	Golden

Table 1 *continued*

Table 1 (*continued*)

Planet	Date (UTC)	Time (UTC)	Telescope	Typical Exposure Time (s)	N _{data}	PNR	Quality
	Nov 03, 2016	18:13:11-21:47:02	Xinglong 60 cm	20	271	0.21	Mediocre
	Dec 10, 2016	17:09:59-21:47:31	Xinglong 60 cm	20	373	0.16	Golden
	Jan 23, 2017	15:41:58-20:10:18	Xinglong 60 cm	22.5	323	0.16	Golden
	Apr 21, 2017	11:42:30-15:01:11	Xinglong 60 cm	40	134	0.18	Golden
WASP-80 b	May 12, 2016	18:38:09-19:57:34	Xinglong 60 cm	25	158	0.14	Golden
	Sep 12, 2017	11:49:35-14:50:21	Xinglong 60 cm	7	336	0.30	Mediocre
XO-2 b	Feb 17, 2017	12:36:48-17:02:57	Xinglong 60/90 cm Schmidt	40	217	0.12	Golden
XO-5 b	Jan 12, 2016	17:58:54-22:10:58	Xinglong 60 cm	100	132	0.24	Mediocre
	Jan 29, 2016	12:20:36-16:06:44	Xinglong 60/90 cm Schmidt	150	84	0.23	Mediocre

Table 2. Photometry of TEMP Targets

Planet	BJD _{TDB}	Relative Flux	Uncertainty	Filter
GJ 436 b	2457456.053648	1.0030	0.0019	R
GJ 436 b	2457456.054238	1.0002	0.0019	R
GJ 436 b	2457456.054840	0.9999	0.0019	R
GJ 436 b	2457456.055430	0.9982	0.0019	R
GJ 436 b	2457456.056032	0.9986	0.0019	R
GJ 436 b	2457456.056622	1.0016	0.0019	R
GJ 436 b	2457456.057224	1.0004	0.0019	R
GJ 436 b	2457456.057815	1.0015	0.0019	R
GJ 436 b	2457456.058416	1.0013	0.0019	R
GJ 436 b	2457456.059018	0.9983	0.0019	R
...

Note: This table is available in its entirety in machine-readable format. A portion of the table is shown here for guidance regarding its form and content. Table 2, 3 and 4 can be downloaded via this [link](#)

Table 3. Transit Mid-Times for TEMP Targets

Planet	Epoch Number	T ₀	σ	O-C
		(BJD _{TDB})	(s)	(s)
GJ 436 b	-42	2454222.616809	65.30	-7.04
GJ 436 b	-41	2454225.260917	71.90	11.29
GJ 436 b	-41	2454225.261190	66.25	34.86
GJ 436 b	-41	2454225.261356	68.20	49.19
GJ 436 b	-39	2454230.548755	70.76	15.32
GJ 436 b	-36	2454238.480865	202.79	51.88
GJ 436 b	-34	2454243.767054	51.72	-86.56
GJ 436 b	-33	2454246.410962	148.03	-85.43
GJ 436 b	-33	2454246.411611	152.83	-29.37
GJ 436 b	-31	2454251.700230	67.85	42.17
GJ 436 b	-20	2454280.782620	21.49	2.27
GJ 436 b	1181	2457456.101184	103.67	0.52
...

Note: This table is available in its entirety in machine-readable format. A portion of the table is shown here for guidance regarding its form and content.

Table 4. System Parameters for TEMP Targets obtained in This Study are Compared with Literature Values.

Parameter	Units	Values	Previous values	Refs	Agreement (σ)
WASP-36					
Stellar Parameters:					
M_*	Mass (M _⊕)	1.030 ^{+0.033} _{-0.036}	1.081 ± 0.034	Mancini et al. (2016)	1.08
R_*	Radius (R _⊕)	0.966 ^{+0.013} _{-0.014}	0.985 ± 0.014	Mancini et al. (2016)	0.99
L_*	Luminosity (L _⊕)	1.202 ^{+0.089} _{-0.081}
ρ_*	Density (cgs)	1.609 ^{+0.042} _{-0.036}	1.595 ± 0.045	Mancini et al. (2016)	0.24
$\log g$	Surface gravity (cgs)	4.4807 ^{+0.0086} _{-0.0085}	4.486 ± 0.009	Mancini et al. (2016)	0.43
T_{eff}	Effective Temperature (K)	6150 ⁺¹¹⁰ ₋₁₀₀	5959 ± 134	Mancini et al. (2016)	1.14
[Fe/H]	Metallicity (dex)	-0.31 ^{+0.20} _{-0.27}	-0.26 ± 0.1	Mancini et al. (2016)	0.17
[Fe/H] ₀	Initial Metallicity	-0.31 ^{+0.18} _{-0.23}
Age	Age (Gyr)	1.01 ^{+1.1} _{-0.68}	1.4 ^{+0.4} _{-0.3}	Mancini et al. (2016)	0.34
EEP	Equal Evolutionary Phase	315 ⁺²⁰ ₋₃₄
A_V	V-band extinction (mag)	0.190 ^{+0.078} _{-0.079}
σ_{SED}	SED photometry error scaling	1.75 ^{+0.69} _{-0.43}
ϖ	Parallax (mas)	2.640 ± 0.033	2.560 ± 0.035	Stassun et al. (2019)	1.66
d	Distance (pc)	378.8 ^{+4.7} _{-4.6}	386.346 ^{+5.261} _{-5.123}	Stassun et al. (2019)	1.09
Planetary Parameters:					
b					
P	Period (days)	1.53736533 ± 0.00000014	1.53736596 ± 0.00000024	Mancini et al. (2016)	2.27
R_P	Radius (R _J)	1.270 ^{+0.018} _{-0.019}	1.327 ± 0.021	Mancini et al. (2016)	2.06
M_P	Mass (M _J)	2.281 ^{+0.070} _{-0.071}	2.361 ± 0.070	Mancini et al. (2016)	0.81
T_C	Time of conjunction (BJD _{TDB})	2455569.83795 ± 0.00011
T_0	Optimal conjunction Time (BJD _{TDB})	2456678.278350 ^{+0.000047} _{-0.000046}
a	Semi-major axis (AU)	0.02635 ^{+0.00028} _{-0.00031}	0.02677 ± 0.00028	Mancini et al. (2016)	1.06
i	Inclination (Degrees)	83.42 ^{+0.12} _{-0.11}	83.15 ± 0.13	Mancini et al. (2016)	1.59
e	Eccentricity	0.0087 ^{+0.0097} _{-0.0061}
ω_*	Argument of Periastron (Degrees)	-43 ± 89

Table 4 *continued*

Table 4 (continued)

Parameter	Units	Values	Previous values	Refs	Agreement (σ)
T_{eq}	Equilibrium temperature (K)	1796^{+32}_{-31}	1733 ± 19	Mancini et al. (2016)	1.73
τ_{circ}	Tidal circularization timescale (Gyr)	$0.01638^{+0.00086}_{-0.00079}$
K	RV semi-amplitude (m/s)	$391.0^{+8.0}_{-8.1}$	391.500 ± 8.300	0.04	0.04
$\log K$	Log of RV semi-amplitude	$2.5922^{+0.0088}_{-0.0091}$
R_P/R_* ..	Radius of planet in stellar radii	$0.13515^{+0.00027}_{-0.00028}$	0.13677 ± 0.00056	Mancini et al. (2016)	2.61
a/R_*	Semi-major axis in stellar radii	$5.862^{+0.050}_{-0.044}$	$5.8480^{+0.0552}_{-0.0542}$	Mancini et al. (2016)	0.2
δ	Transit depth (fraction)	$0.018266^{+0.000074}_{-0.000076}$
$Depth$..	Flux decrement at mid transit	$0.018266^{+0.000074}_{-0.000076}$	0.01916 ± 0.0002	Mancini et al. (2016)	4.19
τ	Ingress/egress transit duration (days)	$0.01577^{+0.00023}_{-0.00024}$
T_{14}	Total transit duration (days)	0.07732 ± 0.00019	0.07566 ± 0.00042	Smith et al. (2012)	3.6
T_{FWHM} ..	FWHM transit duration (days)	0.06155 ± 0.00019
b	Transit Impact parameter	$0.6736^{+0.0055}_{-0.0058}$	$0.6577^{+0.029}_{-0.033}$	Maciejewski et al. (2016)	0.56
b_S	Eclipse impact parameter	$0.6699^{+0.0094}_{-0.012}$
τ_S	Ingress/egress eclipse duration (days)	$0.01561^{+0.00041}_{-0.00049}$
$T_{S,14}$	Total eclipse duration (days)	$0.07716^{+0.00045}_{-0.00065}$
$T_{S,FWHM}$	FWHM eclipse duration (days)	0.06150 ± 0.00023
$\delta_{S,3.6\mu m}..$	Blackbody eclipse depth at $3.6\mu m$ (ppm)	1988 ± 46
$\delta_{S,4.5\mu m}..$	Blackbody eclipse depth at $4.5\mu m$ (ppm)	2515 ± 46
ρ_P	Density (cgs)	$1.380^{+0.050}_{-0.047}$	1.260 ± 0.060	Mancini et al. (2016)	1.57
$log P$	Surface gravity	3.545 ± 0.012
Θ	Saftronov Number	0.0918 ± 0.0023	0.0880 ± 0.0023	Mancini et al. (2016)	1.17
$\langle F \rangle$	Incident Flux (10^9 erg s $^{-1}$ cm $^{-2}$)	$2.36^{+0.17}_{-0.16}$
T_P	Time of Periastron (BJD _{TDB})	$2455569.28^{+0.39}_{-0.38}$
T_S	Time of eclipse (BJD _{TDB})	$2455570.6086^{+0.0094}_{-0.0054}$
T_A	Time of Ascending Node (BJD _{TDB})	$2455569.4537^{+0.0049}_{-0.0047}$
T_D	Time of Descending Node (BJD _{TDB})	$2455570.2242^{+0.0077}_{-0.0039}$
$e \cos \omega_*$	$0.0020^{+0.0095}_{-0.0055}$
$e \sin \omega_*$	$-0.0018^{+0.0056}_{-0.0097}$
$M_P \sin i$..	Minimum mass (M _J)	$2.266^{+0.069}_{-0.071}$
M_P/M_* ..	Mass ratio	0.002116 ± 0.000050
d/R_*	Separation at mid transit	$5.873^{+0.10}_{-0.072}$

Table 4 (continued)

Table 4 (*continued*)

Parameter	Units	Values	Previous values	Refs	Agreement (σ)
P_T	A priori non-grazing transit prob	$0.1473^{+0.0018}_{-0.0025}$
$P_{T,G}$	A priori transit prob	$0.1933^{+0.0024}_{-0.0032}$
P_S	A priori non-grazing eclipse prob	$0.14798^{+0.00081}_{-0.00082}$
$P_{S,G}$	A priori eclipse prob A	0.1942 ± 0.0012
...

Note: This table is available in its entirety in machine-readable format. A portion of the table is shown here for guidance regarding its form and content.

Table 5. Stellar Parameters

Star	M_*	R_*	$\log g$	T_{eff}	[Fe/H]
	(M_\odot)	(R_\odot)	(cgs)	(K)	
GJ 436	$0.426^{+0.027}_{-0.017}$	$0.415^{+0.014}_{-0.010}$	$4.833^{+0.013}_{-0.013}$	3370^{+94}_{-95}	$-0.46^{+0.31}_{-0.24}$
HAT-P-12	$0.719^{+0.016}_{-0.016}$	$0.7084^{+0.0095}_{-0.0095}$	$4.594^{+0.013}_{-0.013}$	4710^{+49}_{-49}	$-0.240^{+0.055}_{-0.062}$
HAT-P-16	$1.187^{+0.058}_{-0.065}$	$1.217^{+0.022}_{-0.022}$	$4.342^{+0.024}_{-0.027}$	6196^{+59}_{-71}	$0.11^{+0.15}_{-0.11}$
HAT-P-18	$0.750^{+0.015}_{-0.014}$	$0.7202^{+0.0095}_{-0.010}$	$4.599^{+0.013}_{-0.013}$	4835^{+39}_{-35}	$0.044^{+0.060}_{-0.051}$
HAT-P-19	$0.863^{+0.029}_{-0.025}$	$0.851^{+0.013}_{-0.013}$	$4.514^{+0.019}_{-0.017}$	5049^{+42}_{-65}	$0.283^{+0.081}_{-0.079}$
HAT-P-20	$0.764^{+0.042}_{-0.051}$	$0.685^{+0.016}_{-0.021}$	$4.650^{+0.018}_{-0.018}$	4622^{+57}_{-49}	$0.23^{+0.25}_{-0.24}$
HAT-P-22	$1.051^{+0.045}_{-0.050}$	$0.990^{+0.018}_{-0.018}$	$4.4687^{+0.0096}_{-0.013}$	5426^{+55}_{-52}	$0.325^{+0.084}_{-0.081}$
HAT-P-24	$1.228^{+0.035}_{-0.036}$	$1.372^{+0.018}_{-0.018}$	$4.252^{+0.017}_{-0.017}$	6488^{+70}_{-68}	$-0.056^{+0.050}_{-0.054}$
HAT-P-27	$0.907^{+0.040}_{-0.036}$	$0.896^{+0.015}_{-0.015}$	$4.491^{+0.024}_{-0.023}$	5162^{+41}_{-41}	$0.210^{+0.097}_{-0.097}$
HAT-P-3	$0.960^{+0.031}_{-0.034}$	$0.8627^{+0.0090}_{-0.012}$	$4.550^{+0.015}_{-0.016}$	5133^{+36}_{-31}	$0.332^{+0.074}_{-0.073}$
HAT-P-30	$1.314^{+0.053}_{-0.056}$	$1.381^{+0.020}_{-0.022}$	$4.277^{+0.019}_{-0.021}$	6216^{+56}_{-48}	$0.155^{+0.077}_{-0.079}$
HAT-P-37	$0.953^{+0.035}_{-0.040}$	$0.8635^{+0.0072}_{-0.0070}$	$4.545^{+0.016}_{-0.019}$	5479^{+37}_{-52}	$0.22^{+0.12}_{-0.12}$
HAT-P-39	$1.414^{+0.039}_{-0.039}$	$1.723^{+0.028}_{-0.028}$	$4.116^{+0.017}_{-0.016}$	6412^{+56}_{-58}	$0.118^{+0.074}_{-0.066}$
HAT-P-4	$1.260^{+0.043}_{-0.042}$	$1.573^{+0.015}_{-0.015}$	$4.145^{+0.015}_{-0.015}$	5927^{+57}_{-47}	$0.258^{+0.070}_{-0.074}$
HAT-P-42	$1.145^{+0.052}_{-0.052}$	$1.27^{+0.11}_{-0.11}$	$4.288^{+0.073}_{-0.067}$	5773^{+45}_{-40}	$0.312^{+0.072}_{-0.074}$
HAT-P-43	$1.042^{+0.036}_{-0.035}$	$1.076^{+0.025}_{-0.025}$	$4.392^{+0.026}_{-0.023}$	5656^{+37}_{-29}	$0.267^{+0.061}_{-0.064}$
HAT-P-5	$1.056^{+0.067}_{-0.067}$	$1.085^{+0.012}_{-0.012}$	$4.391^{+0.029}_{-0.031}$	5844^{+54}_{-52}	$0.14^{+0.18}_{-0.15}$
HAT-P-52	$0.891^{+0.023}_{-0.022}$	$0.886^{+0.031}_{-0.030}$	$4.492^{+0.030}_{-0.029}$	5144^{+47}_{-48}	$0.319^{+0.076}_{-0.078}$
HAT-P-53	$1.078^{+0.036}_{-0.037}$	$1.127^{+0.039}_{-0.036}$	$4.367^{+0.030}_{-0.032}$	5942^{+36}_{-40}	$-0.001^{+0.077}_{-0.064}$
HAT-P-54	$0.706^{+0.027}_{-0.025}$	$0.6703^{+0.0098}_{-0.0097}$	$4.635^{+0.019}_{-0.018}$	4369^{+62}_{-71}	$0.157^{+0.076}_{-0.075}$
HAT-P-56	$1.319^{+0.033}_{-0.033}$	$1.429^{+0.024}_{-0.023}$	$4.248^{+0.017}_{-0.018}$	6564^{+47}_{-46}	$0.11^{+0.14}_{-0.10}$
HAT-P-8	$1.270^{+0.030}_{-0.030}$	$1.491^{+0.016}_{-0.014}$	$4.1956^{+0.0095}_{-0.013}$	6410^{+140}_{-140}	$-0.018^{+0.072}_{-0.056}$
KELT-3	$1.301^{+0.046}_{-0.046}$	$1.583^{+0.036}_{-0.036}$	$4.153^{+0.024}_{-0.024}$	6306^{+36}_{-35}	$0.030^{+0.072}_{-0.066}$
Qatar-4	$0.856^{+0.029}_{-0.030}$	$0.800^{+0.015}_{-0.014}$	$4.565^{+0.018}_{-0.020}$	5174^{+33}_{-35}	$0.095^{+0.076}_{-0.088}$
TrES-1	$0.886^{+0.021}_{-0.022}$	$0.8200^{+0.0079}_{-0.0078}$	$4.5577^{+0.0096}_{-0.010}$	5316^{+43}_{-42}	$0.017^{+0.045}_{-0.041}$
WASP-104	$1.003^{+0.030}_{-0.032}$	$0.9277^{+0.0089}_{-0.0085}$	$4.504^{+0.014}_{-0.016}$	5392^{+69}_{-73}	$0.348^{+0.076}_{-0.076}$
WASP-24	$1.177^{+0.025}_{-0.025}$	$1.312^{+0.019}_{-0.020}$	$4.273^{+0.015}_{-0.014}$	6489^{+89}_{-74}	$-0.37^{+0.12}_{-0.18}$
WASP-28	$1.082^{+0.068}_{-0.071}$	$1.132^{+0.019}_{-0.018}$	$4.365^{+0.027}_{-0.033}$	5976^{+54}_{-60}	$0.06^{+0.17}_{-0.12}$
WASP-36	$1.030^{+0.033}_{-0.036}$	$0.966^{+0.013}_{-0.014}$	$4.4807^{+0.0086}_{-0.0085}$	6150^{+110}_{-100}	$-0.31^{+0.20}_{-0.27}$
WASP-37	$0.926^{+0.039}_{-0.034}$	$1.071^{+0.019}_{-0.018}$	$4.346^{+0.023}_{-0.021}$	5795^{+69}_{-64}	$-0.098^{+0.050}_{-0.060}$
WASP-38	$1.200^{+0.029}_{-0.029}$	$1.368^{+0.014}_{-0.014}$	$4.2450^{+0.0081}_{-0.0083}$	6168^{+57}_{-58}	$-0.001^{+0.065}_{-0.064}$
WASP-43	$0.723^{+0.028}_{-0.031}$	$0.6747^{+0.0086}_{-0.0097}$	$4.639^{+0.010}_{-0.010}$	4286^{+34}_{-40}	$0.28^{+0.19}_{-0.21}$
WASP-52	$0.886^{+0.039}_{-0.043}$	$0.825^{+0.012}_{-0.012}$	$4.553^{+0.019}_{-0.024}$	5070^{+35}_{-40}	$0.37^{+0.13}_{-0.17}$
WASP-56	$1.092^{+0.023}_{-0.023}$	$1.129^{+0.021}_{-0.020}$	$4.371^{+0.018}_{-0.018}$	5646^{+49}_{-48}	$0.160^{+0.057}_{-0.057}$
WASP-60	$1.082^{+0.032}_{-0.031}$	$1.384^{+0.039}_{-0.037}$	$4.190^{+0.026}_{-0.027}$	5926^{+77}_{-76}	$0.023^{+0.067}_{-0.055}$
WASP-65	$1.098^{+0.046}_{-0.052}$	$1.056^{+0.017}_{-0.018}$	$4.430^{+0.016}_{-0.015}$	5749^{+45}_{-48}	$0.447^{+0.086}_{-0.13}$
WASP-80	$0.614^{+0.014}_{-0.012}$	$0.6023^{+0.0066}_{-0.0052}$	$4.6672^{+0.0092}_{-0.011}$	4158^{+41}_{-49}	$-0.011^{+0.034}_{-0.017}$
XO-2	$0.967^{+0.029}_{-0.028}$	$1.004^{+0.013}_{-0.013}$	$4.420^{+0.017}_{-0.016}$	5360^{+50}_{-50}	$0.436^{+0.043}_{-0.046}$
XO-5	$1.053^{+0.064}_{-0.062}$	$1.065^{+0.026}_{-0.026}$	$4.406^{+0.029}_{-0.029}$	5515^{+69}_{-68}	$0.447^{+0.079}_{-0.12}$

Table 6. Planetary Physical and Orbital Parameters for TEMP Targets Obtained in This Study

Planet	<i>P</i>	<i>T</i> ₀	<i>e</i>	<i>R</i> _{<i>P</i>} / <i>R</i> _*	<i>a</i> / <i>R</i> _*	<i>T</i> ₁₄	<i>R</i> _{<i>P</i>}	<i>M</i> _{<i>P</i>}
	(BJD _{TDB})				(days)	(R _J)		(M _J)
GJ 436 b	2.64389565 ^{+0.0000055} _{-0.0000054}	2454346.879828 ^{+0.000099} _{-0.000100}	0.1684 ^{+0.0099} _{-0.0096}	0.08536 ^{+0.00076} _{-0.00064}	14.60 ^{+0.25} _{-0.25}	0.04236 ^{+0.00040} _{-0.00038}	0.3443 ^{+0.014} _{-0.0098}	0.0659 ^{+0.0029} _{-0.0020}
HAT-P-12 b	3.21305856 ^{+0.0000017} _{-0.0000017}	2456003.233217 ^{+0.000059} _{-0.000059}	0.018 ^{+0.018} _{-0.012}	0.14005 ^{+0.00057} _{-0.00059}	11.59 ^{+0.16} _{-0.15}	0.09771 ^{+0.00032} _{-0.00032}	0.965 ^{+0.015} _{-0.015}	0.2070 ^{+0.0077} _{-0.0076}
HAT-P-16 b	2.77596752 ^{+0.0000091} _{-0.0000091}	2455238.56602 ^{+0.00027} _{-0.00027}	0.0400 ^{+0.0030} _{-0.0031}	0.10615 ^{+0.00081} _{-0.00082}	7.24 ^{+0.16} _{-0.17}	0.12804 ^{+0.00092} _{-0.00086}	1.257 ^{+0.028} _{-0.028}	4.13 ^{+0.13} _{-0.15}
HAT-P-18 b	5.50802919 ^{+0.0000068} _{-0.0000068}	2455144.64858 ^{+0.00013} _{-0.00014}	0.00664 ^{+0.0082} _{-0.0046}	0.13826 ^{+0.00092} _{-0.00096}	16.56 ^{+0.24} _{-0.22}	0.11347 ^{+0.00059} _{-0.00059}	0.969 ^{+0.017} _{-0.017}	0.196 ^{+0.012} _{-0.013}
HAT-P-19 b	4.00878735 ^{+0.0000072} _{-0.0000073}	2455528.49236 ^{+0.00119} _{-0.00119}	0.021 ^{+0.024} _{-0.015}	0.1386 ^{+0.0013} _{-0.0013}	11.88 ^{+0.22} _{-0.19}	0.11858 ^{+0.00097} _{-0.00092}	1.148 ^{+0.023} _{-0.023}	0.300 ^{+0.016} _{-0.016}
HAT-P-20 b	2.87531801 ^{+0.0000021} _{-0.0000021}	2456374.820509 ^{+0.000083} _{-0.000083}	0.0157 ^{+0.0027} _{-0.0025}	0.1351 ^{+0.0010} _{-0.0010}	11.40 ^{+0.21} _{-0.19}	0.07780 ^{+0.00052} _{-0.00054}	0.900 ^{+0.025} _{-0.031}	7.37 ^{+0.27} _{-0.33}
HAT-P-22 b	3.21223369 ^{+0.0000043} _{-0.0000043}	2455559.81843 ^{+0.00015} _{-0.00015}	0.0049 ^{+0.0034} _{-0.0032}	0.09883 ^{+0.00064} _{-0.00061}	9.426 ^{+0.075} _{-0.12}	0.1183 ^{+0.00061} _{-0.00057}	0.952 ^{+0.020} _{-0.018}	2.360 ^{+0.067} _{-0.076}
HAT-P-24 b	3.35524419 ^{+0.0000076} _{-0.0000075}	2455626.31703 ^{+0.00021} _{-0.00021}	0.00078 ^{+0.0012} _{-0.00058}	0.09743 ^{+0.00056} _{-0.00056}	7.36 ^{+0.13} _{-0.12}	0.15513 ^{+0.00072} _{-0.00070}	1.301 ^{+0.021} _{-0.021}	0.742 ^{+0.024} _{-0.028}
HAT-P-27 b	3.03957984 ^{+0.0000089} _{-0.0000090}	2455483.89831 ^{+0.00017} _{-0.00017}	0.057 ^{+0.048} _{-0.038}	0.1194 ^{+0.0023} _{-0.0022}	9.54 ^{+0.21} _{-0.20}	0.07118 ^{+0.0015} _{-0.0017}	1.041 ^{+0.027} _{-0.026}	0.645 ^{+0.036} _{-0.036}
HAT-P-3 b	2.89973755 ^{+0.0000018} _{-0.0000018}	2455874.509791 ^{+0.000082} _{-0.000082}	0.019 ^{+0.014} _{-0.010}	0.10995 ^{+0.00056} _{-0.00057}	9.80 ^{+0.14} _{-0.14}	0.08729 ^{+0.00041} _{-0.00041}	0.923 ^{+0.012} _{-0.012}	0.618 ^{+0.017} _{-0.018}
HAT-P-30 b	2.81060217 ^{+0.0000059} _{-0.0000066}	2456131.01029 ^{+0.00026} _{-0.00026}	0.020 ^{+0.019} _{-0.014}	0.1151 ^{+0.0011} _{-0.0010}	6.65 ^{+0.12} _{-0.12}	0.09335 ^{+0.0010} _{-0.0010}	1.546 ^{+0.030} _{-0.030}	0.766 ^{+0.027} _{-0.028}
HAT-P-37 b	2.79744006 ^{+0.0000062} _{-0.0000062}	2455983.43142 ^{+0.00016} _{-0.00016}	0.024 ^{+0.017} _{-0.016}	0.1350 ^{+0.0011} _{-0.0011}	9.52 ^{+0.13} _{-0.15}	0.09615 ^{+0.00073} _{-0.00071}	1.135 ^{+0.014} _{-0.014}	1.18 ^{+0.12} _{-0.12}
HAT-P-39 b	3.5438762 ^{+0.0000011} _{-0.0000011}	2455587.94585 ^{+0.00029} _{-0.00029}	0.0052 ^{+0.0091} _{-0.0040}	0.10092 ^{+0.00069} _{-0.00071}	6.37 ^{+0.11} _{-0.11}	0.1782 ^{+0.0010} _{-0.0010}	1.692 ^{+0.034} _{-0.034}	0.578 ^{+0.078} _{-0.076}
HAT-P-4 b	3.0565240 ^{+0.0000011} _{-0.0000011}	2454499.50645 ^{+0.00032} _{-0.00031}	0.0140 ^{+0.014} _{-0.0095}	0.08362 ^{+0.00061} _{-0.00059}	6.085 ^{+0.077} _{-0.078}	0.17423 ^{+0.00090} _{-0.00091}	1.280 ^{+0.016} _{-0.015}	0.676 ^{+0.025} _{-0.028}
HAT-P-42 b	4.6418374 ^{+0.0000050} _{-0.0000050}	2456110.34894 ^{+0.00056} _{-0.00057}	0.111 ^{+0.12} _{-0.078}	0.08442 ^{+0.0020} _{-0.0016}	9.64 ^{+0.85} _{-0.72}	0.1654 ^{+0.0038} _{-0.0038}	1.040 ^{+0.10} _{-0.089}	0.83 ^{+0.17} _{-0.20}
HAT-P-43 b	3.33268034 ^{+0.0000097} _{-0.0000096}	2456247.32242 ^{+0.00119} _{-0.00021}	0.082 ^{+0.19} _{-0.060}	0.11900 ^{+0.0011} _{-0.00083}	8.84 ^{+0.24} _{-0.21}	0.13551 ^{+0.0013} _{-0.00084}	1.246 ^{+0.031} _{-0.030}	0.34 ^{+0.36} _{-0.34}
HAT-P-5 b	2.78847362 ^{+0.0000037} _{-0.0000037}	2455348.80101 ^{+0.00010} _{-0.00010}	0.027 ^{+0.025} _{-0.019}	0.11399 ^{+0.00081} _{-0.00086}	7.82 ^{+0.18} _{-0.19}	0.12273 ^{+0.00065} _{-0.00066}	1.204 ^{+0.017} _{-0.017}	0.989 ^{+0.053} _{-0.053}
HAT-P-52 b	2.77535988 ^{+0.000014} _{-0.000014}	2447653.65348 ^{+0.00055} _{-0.00058}	0.027 ^{+0.040} _{-0.019}	0.11449 ^{+0.0016} _{-0.0017}	8.98 ^{+0.31} _{-0.29}	0.1006 ^{+0.0012} _{-0.0012}	0.991 ^{+0.043} _{-0.042}	0.812 ^{+0.057} _{-0.069}
HAT-P-53 b	1.96162393 ^{+0.0000070} _{-0.0000072}	2456270.81371 ^{+0.00032} _{-0.00033}	0.063 ^{+0.052} _{-0.039}	0.11117 ^{+0.0013} _{-0.0011}	6.00 ^{+0.20} _{-0.21}	0.11611 ^{+0.0013} _{-0.0011}	1.224 ^{+0.049} _{-0.043}	1.467 ^{+0.076} _{-0.083}
HAT-P-54 b	3.79985429 ^{+0.0000082} _{-0.0000083}	2456656.49059 ^{+0.00015} _{-0.00014}	0.078 ^{+0.024} _{-0.024}	0.15675 ^{+0.00078} _{-0.00080}	13.62 ^{+0.24} _{-0.23}	0.07493 ^{+0.00057} _{-0.00056}	1.022 ^{+0.016} _{-0.016}	0.802 ^{+0.098} _{-0.098}
HAT-P-56 b	2.79083132 ^{+0.0000010} _{-0.0000014}	2447653.29102 ^{+0.00031} _{-0.00031}	0.027 ^{+0.040} _{-0.019}	0.1009 ^{+0.0014} _{-0.0017}	6.41 ^{+0.12} _{-0.12}	0.0928 ^{+0.0014} _{-0.0014}	1.403 ^{+0.031} _{-0.030}	1.81 ^{+0.24} _{-0.24}
HAT-P-8 b	3.07634338 ^{+0.0000054} _{-0.0000054}	2455769.73201 ^{+0.00113} _{-0.00113}	0.0992 ^{+0.011} _{-0.066}	0.09192 ^{+0.00035} _{-0.00034}	6.473 ^{+0.057} _{-0.083}	0.16467 ^{+0.00044} _{-0.00043}	1.334 ^{+0.015} _{-0.013}	1.342 ^{+0.032} _{-0.032}
KELT-3 b	2.7033927 ^{+0.000014} _{-0.000013}	2456426.28703 ^{+0.00045} _{-0.00044}	0.041 ^{+0.041} _{-0.029}	0.0947 ^{+0.0012} _{-0.0012}	5.64 ^{+0.14} _{-0.14}	0.1320 ^{+0.0017} _{-0.0017}	1.458 ^{+0.042} _{-0.041}	1.56 ^{+0.12} _{-0.11}
Qatar-4 b	1.80536494 ^{+0.0000092} _{-0.0000093}	2457899.55166 ^{+0.00020} _{-0.00020}	0.046 ^{+0.064} _{-0.034}	0.13911 ^{+0.0010} _{-0.00096}	7.42 ^{+0.13} _{-0.14}	0.08753 ^{+0.00039} _{-0.00038}	1.083 ^{+0.022} _{-0.021}	5.26 ^{+0.22} _{-0.21}
TrES-1 b	3.03006967 ^{+0.0000011} _{-0.0000011}	2455083.630963 ^{+0.00067} _{-0.00068}	0.0103 ^{+0.011} _{-0.0072}	0.13542 ^{+0.00052} _{-0.00049}	10.322 ^{+0.094} _{-0.095}	0.10466 ^{+0.00032} _{-0.00030}	1.081 ^{+0.012} _{-0.012}	0.698 ^{+0.026} _{-0.025}
WASP-104 b	1.75540646 ^{+0.0000028} _{-0.0000028}	2456788.79015 ^{+0.00011} _{-0.00011}	0.014 ^{+0.019} _{-0.010}	0.12117 ^{+0.00070} _{-0.00068}	6.607 ^{+0.086} _{-0.080}	0.07515 ^{+0.00054} _{-0.00049}	1.094 ^{+0.013} _{-0.013}	1.205 ^{+0.049} _{-0.044}
WASP-24 b	2.34122303 ^{+0.0000060} _{-0.0000059}	2455781.40485 ^{+0.00013} _{-0.00013}	0.0123 ^{+0.013} _{-0.0086}	0.10158 ^{+0.00042} _{-0.00044}	5.971 ^{+0.093} _{-0.088}	0.11418 ^{+0.00057} _{-0.00057}	1.297 ^{+0.022} _{-0.022}	1.082 ^{+0.027} _{-0.028}
WASP-28 b	3.40883577 ^{+0.0000043} _{-0.0000021}	2455754.00767 ^{+0.00031} _{-0.00032}	0.020 ^{+0.023} _{-0.014}	0.1198 ^{+0.0012} _{-0.0011}	8.65 ^{+0.21} _{-0.24}	0.1379 ^{+0.0013} _{-0.0011}	1.319 ^{+0.028} _{-0.026}	0.948 ^{+0.051} _{-0.052}

Table 6 *continued*

Table 6 (continued)

Planet	<i>P</i> (BJD _{TDB})	<i>T</i> ₀	<i>e</i>	<i>R</i> _P / <i>R</i> _*	<i>a</i> / <i>R</i> _*	<i>T</i> ₁₄ (days)	<i>R</i> _P (<i>R</i> _J)	<i>M</i> _P (<i>M</i> _J)
WASP-36 b	1.53736533 ^{+0.0000014} _{-0.0000014}	2456678.27835 ^{+0.000047} _{-0.000046}	0.0087 ^{+0.0097} _{-0.0061}	0.13515 ^{+0.00027} _{-0.00028}	5.862 ^{+0.050} _{-0.044}	0.07732 ^{+0.00019} _{-0.00019}	1.270 ^{+0.018} _{-0.019}	2.281 ^{+0.070} _{-0.071}
WASP-37 b	3.5774729 ^{+0.0000025} _{-0.0000025}	2458096.85691 ^{+0.00119} _{-0.00119}	0.069 ^{+0.025} _{-0.028}	0.11713 ^{+0.0010} _{-0.00095}	8.97 ^{+0.19} _{-0.18}	0.13107 ^{+0.00100} _{-0.00086}	1.220 ^{+0.025} _{-0.024}	1.77 ^{+0.12} _{-0.12}
WASP-38 b	6.8718942 ^{+0.0000037} _{-0.0000036}	2456332.34464 ^{+0.00051} _{-0.00052}	0.0272 ^{+0.0042} _{-0.0040}	0.08518 ^{+0.00062} _{-0.00062}	11.824 ^{+0.094} _{-0.096}	0.2028 ^{+0.0013} _{-0.0013}	1.134 ^{+0.015} _{-0.015}	2.597 ^{+0.045} _{-0.045}
WASP-43 b	0.813474229 ^{+0.0000047} _{-0.0000047}	2455793.247658 ^{+0.00031} _{-0.00031}	0.0059 ^{+0.0053} _{-0.0039}	0.15978 ^{+0.00044} _{-0.00045}	4.883 ^{+0.041} _{-0.038}	0.05166 ^{+0.0016} _{-0.0016}	1.049 ^{+0.014} _{-0.016}	2.054 ^{+0.055} _{-0.060}
WASP-52 b	1.74978344 ^{+0.0000032} _{-0.0000032}	2456960.785928 ^{+0.00061} _{-0.00060}	0.040 ^{+0.022} _{-0.023}	0.16319 ^{+0.00059} _{-0.00061}	7.12 ^{+0.12} _{-0.15}	0.07783 ^{+0.00023} _{-0.00023}	1.310 ^{+0.020} _{-0.019}	0.458 ^{+0.027} _{-0.026}
WASP-56 b	4.6170605 ^{+0.0000028} _{-0.0000028}	2457148.23869 ^{+0.00046} _{-0.00046}	0.138 ^{+0.062} _{-0.060}	0.1039 ^{+0.0021} _{-0.0022}	10.65 ^{+0.21} _{-0.21}	0.1509 ^{+0.0029} _{-0.0027}	1.141 ^{+0.032} _{-0.033}	0.588 ^{+0.040} _{-0.041}
WASP-60 b	4.3050032 ^{+0.0000055} _{-0.0000055}	2456853.41727 ^{+0.00029} _{-0.00029}	0.038 ^{+0.042} _{-0.026}	0.08982 ^{+0.00081} _{-0.00093}	8.26 ^{+0.24} _{-0.24}	0.1497 ^{+0.013} _{-0.014}	1.209 ^{+0.039} _{-0.038}	0.506 ^{+0.052} _{-0.051}
WASP-65 b	2.31142098 ^{+0.0000039} _{-0.0000039}	2456545.23453 ^{+0.0011} _{-0.0011}	0.0126 ^{+0.014} _{-0.0089}	0.11334 ^{+0.00047} _{-0.00045}	7.174 ^{+0.11} _{-0.080}	0.111507 ^{+0.00038} _{-0.00037}	1.165 ^{+0.020} _{-0.020}	1.719 ^{+0.062} _{-0.064}
WASP-80 b	3.06785314 ^{+0.0000044} _{-0.0000043}	2456416.864196 ^{+0.00025} _{-0.00025}	0.0107 ^{+0.011} _{-0.075}	0.17212 ^{+0.00042} _{-0.00043}	12.55 ^{+0.11} _{-0.13}	0.08901 ^{+0.00015} _{-0.00015}	1.0091 ^{+0.011} _{-0.0095}	0.571 ^{+0.020} _{-0.020}
XO-2 b	2.61585881 ^{+0.0000029} _{-0.0000029}	2454762.4765 ^{+0.00012} _{-0.00012}	0.0095 ^{+0.0092} _{-0.0065}	0.10372 ^{+0.00062} _{-0.00064}	7.87 ^{+0.13} _{-0.12}	0.11294 ^{+0.00048} _{-0.00047}	1.013 ^{+0.018} _{-0.017}	0.589 ^{+0.015} _{-0.014}
XO-5 b	4.18775571 ^{+0.0000049} _{-0.0000049}	2454510.79378 ^{+0.00024} _{-0.00024}	0.0101 ^{+0.012} _{-0.0072}	0.1022 ^{+0.0010} _{-0.00073}	10.45 ^{+0.29} _{-0.28}	0.12765 ^{+0.00083} _{-0.00073}	1.058 ^{+0.033} _{-0.032}	1.188 ^{+0.053} _{-0.052}

5. ACKNOWLEDGMENTS

We thank Jason Eastman for his useful discussions. We also would like to thank Metrics for advice on figure designs that has led to a considerable improvement of the manuscript. S.W. acknowledges support from Indiana University, Yale University, and the Heising-Simons Foundation. M.R. is supported by the National Science Foundation Graduate Research Fellowship Program under Grant Number DGE-1752134. TCH acknowledges financial support from the National Research Foundation (NRF; No. 2019R1I1A1A01059609). M.B. and Y.W. thank the support of the National Natural Science Foundation of China (Grant No. 12073092). Y.W. thanks the fellowship of the China Postdoctoral Science Foundation (Grant No. 2020M672936). H.Z. thanks the support of the National Natural Science Foundation of China (Grant No. 12073010). This work is supported by the National Natural Science Foundation of China (NSFC) (11803055), the Joint Research Fund in Astronomy (U1731125, U1731243, U1931132) under cooperative agreement between the NSFC and Chinese Academy of Sciences (CAS), the 13th Five-year Informatization Plan of Chinese Academy of Sciences (No. XXH-13514, XXH13503-03-107). This work is supported by Astronomical Big Data Joint Research Center, co-founded by National Astronomical Observatories, Chinese Academy of Sciences and Alibaba Cloud. We acknowledge the support of the staff of the Xinglong 60 cm telescope. This work was partially supported by the Open Project Program of the Key Laboratory of Optical Astronomy, National Astronomical Observatories, Chinese Academy of Sciences.

REFERENCES

- Addison, B. C., Wang, S., Johnson, M. C., et al. 2018, AJ, 156, 197
- Addison, B. C., Wright, D. J., Nicholson, B. A., et al. 2020, MNRAS, 502, 3704
- Agol, E. & Deck, K. 2016, ApJ, 818, 177
- Agol, E., Steffen, J., Sari, R., & Clarkson, W. 2005, MNRAS, 359, 567
- Albrecht, S., Winn, J. N., Johnson, J. A., et al. 2012, ApJ, 757, 18
- Alonso, R., Brown, T. M., Torres, G., et al. 2004, ApJL, 613, L153
- Alsubai, K. A., Parley, N. R., Bramich, D. M., et al. 2013, AcA, 63, 465
- Auvergne, M., Bodin, P., Boisnard, L., et al. 2009, A&A, 506, 411
- Bakos, G. Á., Noyes, R. W., Kovács, G., et al. 2004, PASP, 116, 266
- Bakos, G. Á., Csabry, Z., Penev, K., et al. 2013, PASP, 125, 154
- Batygin, K., Bodenheimer, P. H., & Laughlin, G. P. 2016, ApJ, 829, 114
- Becker, J. C., Vanderburg, A., Adams, F. C., et al. 2015, ApJL, 812, L18
- Bertin, E., Arnouts, S. 1996, A&AS, 117, 393B
- Bianchi, L., Herald, J., Efremova, B., et al. 2011, Ap&SS, 335, 161
- Boley, A. C., Granados Contreras, A. P., & Gladman, B. 2016, ApJL, 817, L17
- Borucki, W. J., Koch, D., Basri, G., et al. 2010, Science, 327, 977
- Borucki, W. J., Koch, D., Jenkins, J., et al. 2009, Science, 325, 709
- Bouma, L. G., Winn, J. N., Baxter, C., et al. 2019, AJ, 157, 217
- Brahm, R., Nielsen, L. D., Wittenmyer, R. A., et al. 2020, AJ, 160, 235
- Carter, J. A., & Winn, J. N. 2010, ApJ, 709, 1219
- Cañas, C. I., Wang, S., Mahadevan, S., et al. 2019, ApJL, 870, L17
- Cañas, C. I., Stefansson, G., Monson, A. J., et al. 2019, ApJL, 877
- Charbonneau, D., Allen, L. E., Megeath, S. T., et al. 2005, ApJ, 626, 523
- Charbonneau, D., Brown, T. M., Noyes, R. W., & Gilliland, R. L. 2002, ApJ, 568, 377
- Cincotta, P. M., & Simó, C. 1999, Celestial Mechanics and Dynamical Astronomy, 73, 195
- Cincotta, P. M., & Simó, C. 2000, A&AS, 147, 205
- Cincotta, P. M., Giordano, C. M., & Simó, C. 2003, Physica D Nonlinear Phenomena, 182, 151
- Claret, A. 2018, A&A, 618, A20
- Cortés-Zuleta, P., Rojo, P., Wang, S., et al. 2020, A&A, 636, A98
- Cutri, R. M., Et, A. 2013, Vizier Online Data Catalog, II/328
- Cutri, R. M., Skrutskie, M. F., van Dyk, S., et al. 2003, The IRSA 2MASS All-Sky Point Source Catalog, NASA/IPAC Infrared Science Archive.
- Davis, A. B., Wang, S., Jones, M., et al. 2020, AJ, 160, 229
- Deming, D., & Seager, S. 2017, arXiv:1701.00493
- Deming, D., Seager, S., Richardson, L. J., & Harrington, J. 2005, Nature, 434, 740
- Eastman, J., Gaudi, B. S., Agol, E. 2013, PASP, 125, 83
- Eastman, J., Siverd, R., & Gaudi, B. S. 2010, PASP, 122, 935
- Eastman, J., Rodriguez, J. E., Agol, E., et al. 2019, Arxiv E-prints, arXiv:1907.09480
- Eastman, J. 2017, Astrophysics Source Code Library. ascl:1710.003
- Fulton, B., Shporer, A., Winn, j., et al. 2011, AJ, 142, 84
- Gaia, C., Brown, A. G. A., Vallenari, A., et al. 2016, A&A, 595, A2
- Gaia Collaboration, Brown, A. G. A., Vallenari, A., et al. 2018, A&A, 616, A1
- Gardner, J. P., Mather, J. C., Clampin, M., et al. 2006, SSRv, 123, 485
- Gelman, A. & Rubin, D. B. 1992, Statistical Science, 7, 457
- Gillon, M., Triaud, A. H. M. J., Fortney, J. J., et al. 2012, A&A, 542, A4
- Greiss, S., Steeghs, D., Gänsicke, B. T., et al. 2012, AJ, 144, 24
- Henden, A. A., Templeton, M., Terrell, D., et al. 2016, Vizier Online Data Catalog, II/336
- Hinse, T. C., Christou, A. A., Alvarellos, J. L. A., & Go'zdziewski, K. 2010, MNRAS, 404, 837
- Holman, M. J., & Murray, N. W. 2005, Science, 307, 1288
- Holman, M. J., Winn, J. N., Latham, D. W., et al. 2006, ApJ, 652, 1715
- Holt, J. R. 1893, Astronomy and Astro-Physics (formerly The Sidereal Messenger), 12, 646
- Howell, S. B., Sobeck, C., Haas, M., et al. 2014, PASP, 126, 398
- Huang, C. X., Petrovich, C., & Deibert, E. 2017, AJ, 153, 210
- Huang, C. X., Quinn, S. N., Vanderburg, A., et al. 2020, ApJL, 892, L7

- Hébrard, G., Bouchy, F., Pont, F., et al. 2008, A&A, 488, 763
- Hébrard, G., Díaz, R. F., Correia, A. C. M., et al. 2020, A&A, 640, A32
- Hög, E., Fabricius, C., Makarov, V. V., et al. 2000, A&A, 355, L27
- Irwin, J., Charbonneau, D., Nutzman, P., & Falco, E. 2009, *Transiting Planets*, 253, 37
- Jones, M. I., Brahm, R., Espinoza, N., et al. 2019, A&A, 625, A16
- Jordán, A., Brahm, R., Espinoza, N., et al. 2020, AJ, 159, 145
- Knutson, H. A., Lewis, N., Fortney, J. J., et al. 2012, ApJ, 754, 22
- Kreidberg, L., Bean, J. L., Désert, J.-M., et al. 2014, Nature, 505, 69
- Laughlin G., Crismani M., Adams F. C., 2011, 729(1), L7
- Lucy, L. B. & Sweeney, M. A. 1971, AJ, 76, 544
- Maciejewski, G., Dimitrov, D., Mancini, L., et al. 2016, AcA, 66, 55
- Macqueen, J. B. 1967, 281-297, "Some Methods for Classification and Analysis of Multivariate Observations," In: Proceedings of 5th Berkeley Symposium on Mathematical Statistics and Probability, University of California Press, Berkeley
- Mallonn, M., Von, E. C., Herrero, E., et al. 2019, A&A, 622, A81
- Mancini, L., Kemmer, J., Southworth, J., et al. 2016, MNRAS, 459, 1393
- McCullough, P. R., Stys, J. E., Valenti, J. A., et al. 2005, PASP, 117, 783
- McLaughlin, D. B. 1924, ApJ, 60, 22
- Mermilliod, J. -C. 1994, Vizier Online Data Catalog, II/193
- Millholland, S., Wang, S., & Laughlin, G. 2016, ApJL, 823, L7
- Montalto, M., Gregorio, J., Boué, G., et al. 2012, MNRAS, 427, 2757. doi:10.1111/j.1365-2966.2012.21926.x
- Nascimbeni, V., Piotto, G., Bedin, L. R., et al. 2011, A&A, 527, A85
- Neuhäuser, R., Errmann, R., Berndt, A., et al. 2011, Astronomische Nachrichten, 332, 547
- Paunzen, E. 2015, A&A, 580, A23
- Penev, K., Bouma, L. G., Winn, J. N., & Hartman, J. D. 2018, AJ, 155, 165
- Pepper, J., Pogge, R. W., DePoy, D. L., et al. 2007, PASP, 119, 923
- Pollacco, D. L., Skillen, I., Collier Cameron, A., et al. 2006, PASP, 118, 1407
- Press W. H., Flannery B. P., Teukolsky S. A., Vetterling W. T., 1992, Numerical Recipes in Fortran 77, 2nd edn. Cambridge Univ. Press, Cambridge
- Pál, A., & Kocsis, B. 2008, MNRAS, 389, 191
- Queloz, D., Eggenberger, A., Mayor, M., et al. 2000, A&A, 359, L13
- Rein, H. & Liu, S.-F. 2012, A&A, 537, A128
- Rein, H. & Spiegel, D. S. 2015, MNRAS, 446, 1424
- Ricker, G. R., Winn, J. N., Vanderspek, R., et al. 2015, Journal of Astronomical Telescopes, Instruments, and Systems, 1, 014003
- Rossiter, R. A. 1924, ApJ, 60, 15
- Schlafly, E. F., Finkbeiner, D. P. 2011, ApJ, 737, 103
- Schlaufman, K. C., & Winn, J. N. 2013, ApJ, 772, 143
- Schlesinger, F. 1910, Publications of the Allegheny Observatory of the University of Pittsburgh, 1, 123
- Seager, S., & Hui, L. 2002, ApJ, 574, 1004
- Seager, S. & Mallén-Ornelas, G. 2003, ApJ, 585, 1038
- Smith, A. M. S., Anderson, D. R., Collier, C. A., et al. 2012, AJ, 143, 81
- Southworth, J., Maxted, P. F. L., Smalley, B. 2004, MNRAS, 349, 547
- Southworth, J., Maxted, P. F. L., Smalley, B. 2004, MNRAS, 351, 1277
- Southworth, J., Hinse, T. C., Jørgensen, U. G., et al. 2009, MNRAS, 396, 1023
- Stassun, K. G., & Torres, G. 2018, ApJ, 862, 61
- Stassun, K. G., Oelkers, R. J., Paegert, M., et al. 2019, AJ, 158, 138
- Steffen, J. H., Ragozzine, D., Fabrycky, D. C., et al. 2012, Proceedings of the National Academy of Sciences of the United States of America, 109, 7982
- Talens, G. J. J., Spronck, J. F. P., Lesage, A.-L., et al. 2017, A&A, 601, A11
- Ter Braak C. J. F. 2006, Stat. Comput., 16, 239
- Thorngren, D. P., Fortney, J. J., et al. 2018, AJ, 155, 214T
- Udalski, A., Paczynski, B., Zebrun, K., et al. 2002, AcA, 52, 1
- Wang, S., Addison, B., Fischer, D. A., et al. 2018a, AJ, 155, 70
- Wang, S., Jones, M., Shporer, A., et al. 2019, AJ, 157, 51
- Wang, S., Wang, X.-Y., Wang, Y.-H., et al. 2018b, AJ, 156, 181
- Wang, S., Wu, D.-H., Barclay, T., et al. 2017, arXiv:1704.04290
- Wang, S., Zhang, H., Zhou, J.-L., et al. 2014, ApJS, 211, 26
- Wang, X.-Y., Wang, S., Hinse, T. C., et al. 2018, PASP, 130, 064401
- Wang, Y.-H., Wang, S., Liu, H.-G., et al. 2017, AJ, 154, 49

- Wang, Y.-H., Wang, S., Hinse, T. C., et al. 2019, AJ, 157, 82
- Wheatley, P. J., West, R. G., Goad, M. R., et al. 2018, MNRAS, 475, 4476
- Winn, J. N., & Fabrycky, D. C. 2015, ARA&A, 53, 409
- Wittenmyer, R. A., Clark, J. T., Zhao, J., et al. 2019, MNRAS, 484, 5859
- Wittenmyer, R. A., Wang, S., Horner, J., et al. 2013, ApJS, 208, 2
- Wu, D.-H., Wang, S., Zhou, J.-L., et al. 2018, AJ, 156, 96
- Zacharias, N., Finch, C. T., Girard, T. M., et al. 2012, Vizier Online Data Catalog, I/322A
- Zhou, G., Rodriguez, J. E., Collins, K. A., et al. 2016, AJ, 152, 136
- Zhou, X., Chen, J., Xu, W., et al. 1999, PASP, 111, 909
- Zhou, X., Jiang, Z., Xue, S., et al. 2001, ChJA&A, 1,372